Ligand Non-Innocence and Proton Channel Promote Cobalt-Catalyzed Electrochemical CO_2 Reduction with Predominant CO Selectivity

Ayan Bera, [‡, a] Sarah Bimmermann, [‡, b] Dibya Jyoti Barman, [a] Leon Gerndt,[a] Thomas Lohmiller,[a,c] Kaltum Abdiaziz,[d] Maylis Orio,[h] Alexander Schnegg,[d] Kara L. Bren,[g] Dennis G. H. Hetterscheid,[e] Michael Römelt,*[,a] Ulf-Peter Apfel,* [b,f] and Kallol Ray*[,a]

[a]Department of Chemistry, Humboldt-Universität zu Berlin, Brook-Taylor-Straße 2, 12489 Berlin, Germany

[b]Faculty of Chemistry & Biochemistry, Ruhr-Universität Bochum, Universitätsstraße 150, 44801 Bochum, Germany

[c]EPR4Energy Joint Lab, Department Spins in Energy Conversion and Quantum Information Science, Helmholtz Zentrum Berlin für Materialien und Energie GmbH, Albert-Einstein-Straße 16, 12489 Berlin, Germany

[d]Max Planck Institute for Chemical Energy Conversion, 34-36 Stiftstraße, Mülheim an der Ruhr, 45470, Germany

[e]Leiden Institute of Chemistry, Leiden University, P.O. Box 9502, 2300 RA Leiden, The Netherlands

[f]Department of Electrosynthesis, Fraunhofer UMSICHT, Osterfelder Straße 3, 46047 Oberhausen, Germany

[g]Department of Chemistry, University of Rochester, Rochester, New York 14627-0216, United States

[h]Aix-Marseille Univ, CNRS, Centrale Marseille, iSm2 Marseille, France

ABSTRACT: Enzymes and heterogenous catalysts for CO_2 reduction reactions (CO_2RR) use secondary interactions between metal sites and protein-derived coordination spheres to control the precise transfer of protons and electrons to minimize overpotential and maximize selectivity over the competitive hydrogen evolution reaction. We now report a molecular cobalt (II) complex **[1-Co]$^{2+}$** that uses a similar strategy under homogenous condition through the use of a redox non-innocent ligand, Hbbpya, containing two 2,2′-bipyridine chelating groups linked by a -NH moiety. By acting as a structural anchor to form a hydrogen-bonded network of four phenol groups, the -NH group enables efficient binding and protonation of CO_2 at a cobalt center to form CO under electrocatalytic conditions at a moderate overpotential and with high selectivity. Methylation of the -NH group in **[2-Co]$^{2+}$** results in a loss of CO_2RR selectivity and increased production of hydrogen. The complexes **[1-Co]$^{2+}$** and **[2-Co]$^{2+}$**, and their one and two electron-reduced counterparts are extensively characterized by X-ray diffraction, cyclic voltammetry, electron paramagnetic resonance and density functional theoretical calculations. The electronic structure of the catalytically active doubly-reduced **[1-Co]^{0}** and **[2-Co]^{0}** can be best described as containing a cobalt(I) center and a mono reduced ligand system. Most importantly, in stoichiometric reactions, due to the presence of an efficient proton relay, **[1-Co]^{0}** performs fast two-electron reduction of CO_2 to form **[1-Co]$^{2+}$** and CO, thereby, avoiding the formation of the high-energy CO_2 radical anion, reminiscent of the CO_2RR mechanism proposed in NiFe-carbon monoxide dehydrogenase. In contrast, a one-electron chemistry prevails in reactions of **[2-Co]^{0}** and CO_2.

1. Introduction

The transformation of CO_2 into valuable carbon-based fuels through reduction presents a sustainable approach to addressing global energy demands and reducing greenhouse gas emissions.[1-5] Efficient catalysts are necessary that can selectively perform CO_2 reduction reactions (CO_2RR) over the kinetically and thermodynamically competitive hydrogen evolution reaction (HER). Furthermore, selectivity is also desirable as CO_2 reduction can lead to a variety of products in a fairly narrow range of potential (Scheme 1).[6-7] Toward these goals, design and detailed study of homogeneous molecular catalysts is of particular relevance, as it may present us with an opportunity to understand the individual electron and proton transfer steps involved in the complex multielectron redox transformations required to convert CO_2 to value added products. In this regard, the small size of the molecular systems and the fact that they can be tuned with a level of atomic precision offer potential advantages over the related biological[5] and heterogeneous catalysts[8-12] for CO_2RR. However, despite advances in the development of molecular catalysts with highly specialized ligand scaffolds, including cyclams,[13-17] porphyrins,[18-26] phthalocyanines,[9, 27] corroles,[28-29] and polypyridines,[30-37] the factors that lead to high product selectivity, low overpotential, high turnover number, and compatibility with aqueous electrolytes while avoiding off-pathway HER during homogenous CO_2RR, are not well understood.

Detailed efforts have also been investigated in understanding the role of the ancillary ligands in the catalytic cycles for multielectron, multiproton redox

Scheme 1. Overview of the Generation of Different Reduced C1 Products during CO_2RR.

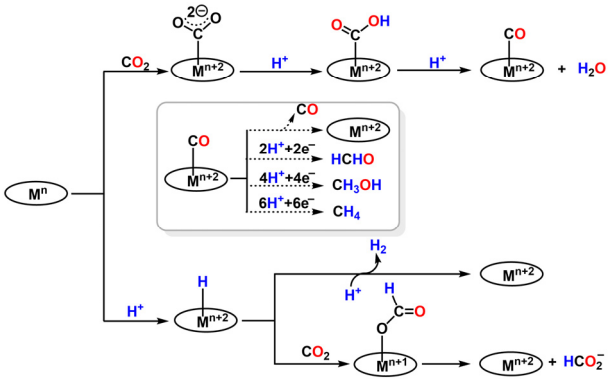

transformations of CO_2. In particular, in presence of redox-active moiety in the ligand backbone,[38-42] preferential electron capture may occur in the ligand-based orbitals, which will reduce the nucleophilicity of the metal center, thereby, decreasing the probability of metal-hydride formation, which is a prerequisite[43-47] for the formation of formate or H_2 products (Scheme 1). The use of redox-active ligands can also introduce basic sites capable of increasing the local proton concentration near the catalytic center,[22, 48-49] thereby, improving catalyst performance and selectivity. Otherwise poorly basic positions in the ligand-backbone can become proton-responsive upon ligand-based reduction and may function as proton relays,[50-54] thereby affecting the rate of proton assisted multielectron processes, like proton or CO_2 reductions. [55-57]

In this work, we compare the electrocatalytic CO_2RR activities and selectivities of two molecular catalysts **[1-Co]$^{2+}$** and **[2-Co]$^{2+}$** (Scheme 2) that contain a Co(II)-center that is chelated to two 2,2′-bipyridine (bpy) groups linked by -NH or -N(CH_3) groups, respectively. Notably, the iron,[58] cobalt,[59] and copper [60]complexes based on the -NH bridged ligand, N,N-bis(2,2′-bipyrid-6-yl) amine (Hbbpya), were previously shown by one of us as efficient catalysts for water oxidation. The water oxidation mechanism of the [Cu(Hbbpya)]$^{2+}$ complex,[60] in particular, has been analyzed in details by theoretical studies. The deprotonated complex [Cu^{II}(bbpya) (H_2O)]$^+$ is proposed to be the predominant species under catalytic conditions, and the Cu centre retained its +2 oxidation state throughout the catalytic cycle, thereby, highlighting the non-innocent character of the Hbbpya ligand. The cobalt complex of a similar ligand system with a -N(C_4H_9) bridge between the two bipyridine units has been utilized by Mulfort and coworkers[61] for H_2 production. An intramolecular proton transfer step that generates the H–H bond between the metal hydride and ligand proton is proposed to be vital for catalytic efficiency.

The ability of the redox-active bipyridine components and nitrogen groups, to participate in electron and proton transfer steps, inspired us to investigate the electrocatalytic CO_2RR capabilities of **[1-Co]$^{2+}$** and **[2-Co]$^{2+}$**. While the incorporation of the redox-active bipyridine moieties within the ligand scaffold can lead to metal–ligand orbital mixing and delocalization of electron density away from the metal centre to favour CO_2 reduction over H^+ reduction, the proton channels mediated by the bridging -NH and -NCH_3 groups can impact product selectivity. Interestingly, although both **[1-Co]$^{2+}$** and **[2-Co]$^{2+}$** can perform CO_2RR with moderate overpotential (500 mV), only **[1-Co]$^{2+}$** exhibits the high selectivity for CO production (~95%) in CH_3CN by employing phenol as a proton donor. The mechanism of CO_2RR has been clarified using theoretical and kinetic studies of the overall catalytic reaction as well as of each step in the catalytic cycle and by chemical and electrochemical reductions of **[1-Co]$^{2+}$** to

Scheme 2. Electronic and Geometric Structures of (A) [1-Co]$^{2+}$, (B) [(bbpya)Co]$^+$, and (C) [2-Co]$^{2+}$ Investigated in the Present Study for Electrocatalytic CO_2RR.

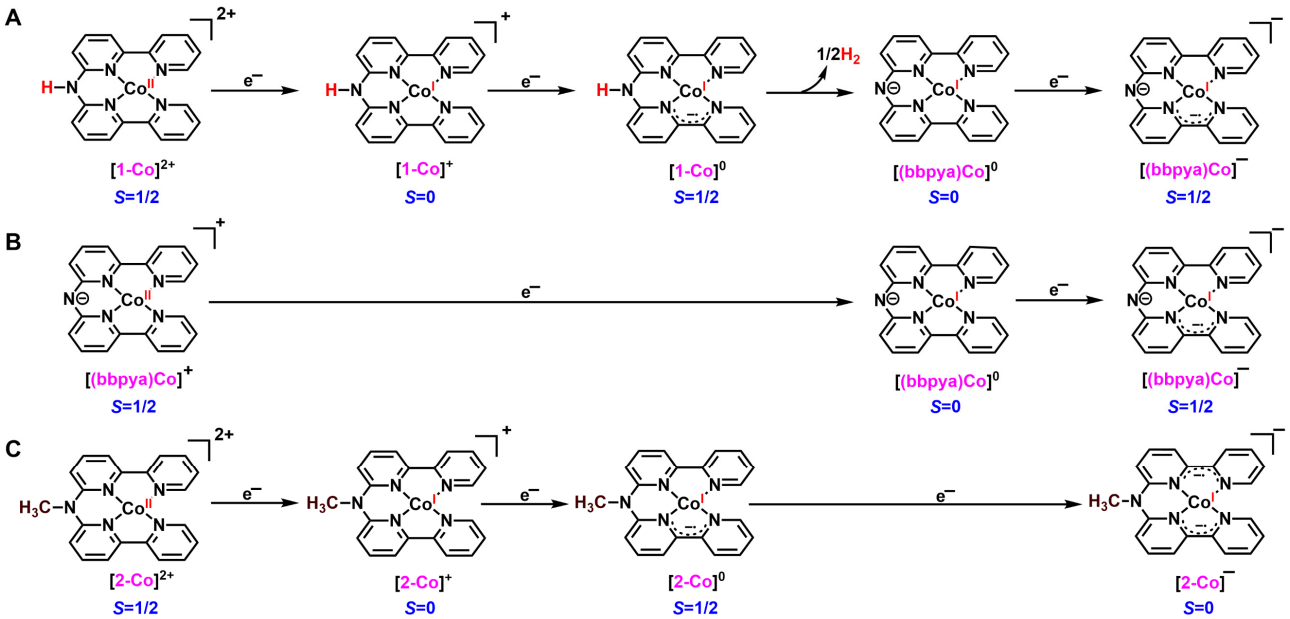

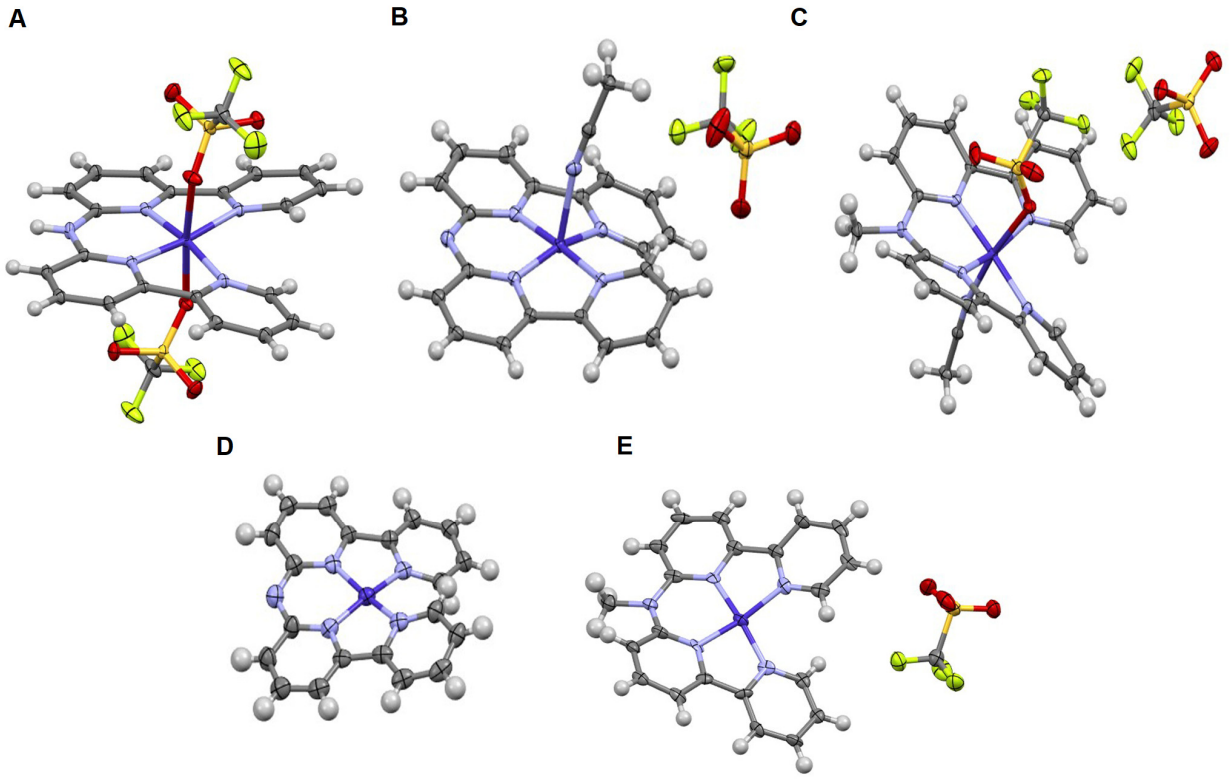

Figure 1. Single crystal X-ray diffraction (XRD) structures of (A) **[1-Co]$^{2+}$**, (B) **[(bbpya)Co]$^{+}$**, (C) **[2-Co]$^{2+}$**, (D) **[(bbpya)Co]^{0}**, and (E) **[2-Co]$^{+}$**. Thermal ellipsoids are drawn at the 50% probability level. See Table S1-S2 for the details of the crysatallographic data.

access the catalytically active doubly-reduced species **[1-Co]^{0}**, which interacts with CO_2 to form **[1-Co-CO_2]**. The difference in CO_2RR selectivity in **[1-Co]$^{2+}$** and **[2-Co]$^{2+}$** is attributed to the requirement for both an efficient proton shuttle and a redox non-innocent ligand for CO_2 to CO conversion. A hydrogen bonded phenol containing network mediated by the -NH bridge in **[1-Co]$^{2+}$** drives the efficient protonation of **[1-Co-CO_2]** leading to high selectivity for CO_2RR over HER.

2. Results and Discussion

Ligand Synthesis and Characterization.

The ligand N, N-bis(2,2′-bipyrid-6-yl) amine (Hbbpya) has been synthesized in three steps (Scheme S1, Figure S1-S4 for detailed characterization) with a slightly modified procedure as described previously.[59] The deprotonated ligand (bbpya) was synthesized by adding 2 equivalents of potassium tert-butoxide (KO^{t}Bu) in a dimethyl formamide (DMF) solution of Hbbpya (Scheme S2)(see SI for detailed synthetic procedure). The synthesis of bbpya, was confirmed by ^{1}H, ^{13}C nuclear magnetic resonance (NMR) and attenuated total reflectance infrared (ATR-IR) spectroscopies (Figures S5-S7). Notably, bbpya lacks the N-H signatures of Hbbpya in form of a resonance at 9.91 ppm in ^{1}H NMR and a N-H vibration at 3325 cm^{-1} in ATR-IR. The ligand Mebbpya, N-([2,2'-bipyridin]-6-yl)-N-methyl-[2,2'-bipyridin]-6-amine, was synthesized by the reaction of Hbbpya with KO^{t}Bu and methyl iodide (MeI) in (DMF) under a N_2 atmosphere (Scheme S3, Figure S8 for characterization).

Synthesis and Characterization of the Co(II) Complexes.

The syntheses of the **[1-Co]$^{2+}$** and **[2-Co]$^{2+}$** complexes have been achieved by stirring the corresponding ligands Hbbpya and Mebbpya, respectively, with an equivalent amount of cobalt triflate Co^{II}(OTf)$_2$ in acetonitrile (MeCN) for 12 hours followed by removal of the solvent under vacuum to yield the complexes as light yellow powders in ~77% yield (see SI for detailed synthetic procedure). The complexes were purified by recrystallisation from MeCN/diethylether (Et_2O). Single crystals suitable for X-ray analysis of the resulting complexes were obtained by vapor diffusion of Et_2O into saturated solutions of the complexes in MeCN. The solid-state structures of both **[1-Co]$^{2+}$** and **[2-Co]$^{2+}$** exhibit a distorted octahedral geometry with four N atoms from the bipyridine moieties coordinated at the equatorial position (Figure 1). In the case of **[1-Co]$^{2+}$**, both the axial positions are occupied by the triflate (OTf) anions (Figure 1A), whereas for **[2-Co]$^{2+}$**, the axial positions are coordinated by one MeCN and one $^{-}$OTf ion, respectively (Figure 1C). ^{19}F NMR of the complexes in CD_3CN (Figures S9-S10) revealed a peak at -78 ppm corresponding to free $^{-}$OTf anions, suggesting that in solution, the $^{-}$OTf ions are quickly exchanged with solvent MeCN molecules in the axial positions. In **[2-Co]$^{2+}$**, the four N atoms from the bipyridine moieties in the equatorial plane form a torsion angle (N1-N2-N3-N4) of 11.20°, which is slightly higher compared to that in **[1-Co]$^{2+}$** (9.68°) (Figure S11A-B). Interestingly, the two bipyridine planes in **[2-Co]$^{2+}$** form an angle of 33.94° (Figure S12B) with each other around the cobalt center,

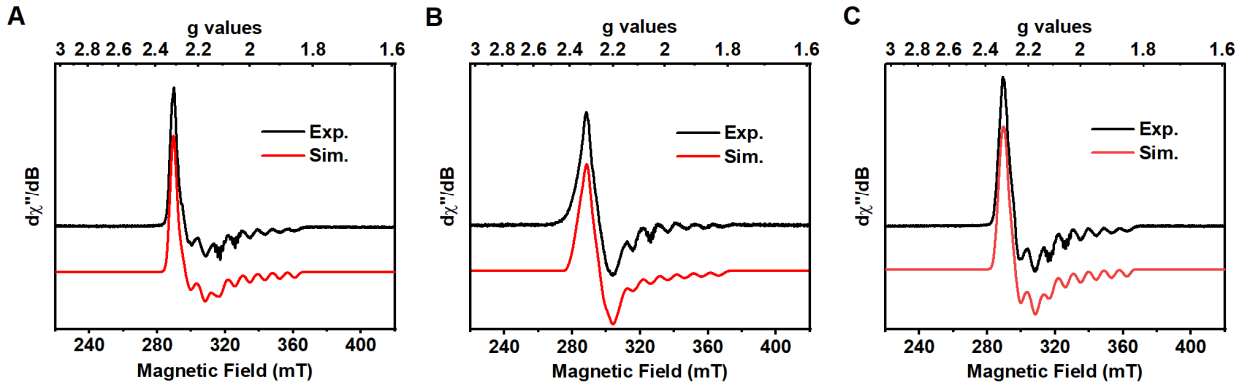

Figure 2. X-band EPR spectra of (A) **[1-Co]²⁺**, (B) **[(bbpya)Co]⁺** and (C) **[2-Co]²⁺** in frozen butyronitrile solutions. Conditions: microwave frequency~ 9.37GHz, microwave power 0.016mW, modulation amplitude 0.5mT, temperature 14K. Experimental spectra are shown in black and the simulations in red. The following parameters were used for the simulations: (A) g_x = 2.254, g_y = 2.220, g_z = 2.026, lwpp = [2.65 0.95], |A_{Co} |, /MHz= 27, 91, 249; (B) g_x = 2.301, g_y = 2.226, g_z = 2.017, lwpp = 0.89 , |A_{Co} |, /MHz= 19, 21, 280 , anisotropic broadenings (in MHz): HStrain(1) = 309 , HStrain(2) = 144 , Hstrain(3) = 50 ; (C) g_x = 2.271, g_y = 2.215, g_z = 2.025 , lwpp = 2.55 , |A_{Co} |, /MHz= 36, 63, 258 .

implying a more distorted structure in contrast to **[1-Co]²⁺**, where the angle is only 11.96° (Figure S12A). Moreover, for **[2-Co]²⁺**, the Co atom is 0.151 Å out of plane from the mean plane connecting the four coordinating nitrogen atoms from the bipyridine units, whereas, in case of **[1-Co]²⁺**, it's only 0.026 Å. Thus, **[2-Co]²⁺** exhibits a greater degree of distortion in the ligand framework compared to **[1-Co]²⁺**. The average Co-N bond distances in both **[1-Co]²⁺** and **[2-Co]²⁺** are, however, identical at 1.946(1) Å, which falls within the range of reported polypyridine cobalt(II) complexes(Table 1).[62] The ^{1}H NMR spectra of **[1-Co]²⁺** and **[2-Co]²⁺** show broad signals in the spectral window of +30 to -10 ppm, demonstrating the paramagnetic nature of the complexes (Figure S13-S14). Similar electronic structures for **[2-Co]²⁺** and **[1-Co]²⁺** in their ground state, in spite of the slight differences in their geometrical structures, were corroborated by the measurement of X-band EPR spectra, which were recorded in frozen butyronitrile solutions at 14K. Both **[1-Co]²⁺** and **[2-Co]²⁺** exhibit an axial EPR spectrum (Figure 2A, 2C), in which hyperfine splitting due to ^{59}Co (I = 7/2) completely resolved along the z direction, resulting in the g_z component splitting into eight lines. Simulations of the spectra unveiled optimised g tensors with similar principal components [g_x, g_y, g_z] = [2.254, 2.220, 2.026] and [2.271, 2.215, 2.025] for **[1-Co]²⁺** and **[2-Co]²⁺**, respectively, indicative of a low spin (S = 1/2) Co(II) configuration with a dz² ground state. For **[1-Co]²⁺**, cobalt hyperfine coupling constants [A_x, A_y, A_z] = [27, 91, 249] MHz were determined, which is similar to those obtained for **[2-Co]²⁺** ([36, 63, 258] MHz, Table 2.) Additionally, super-hyperfine coupling due to two equivalent ^{14}N (I = 1) nuclei along the z direction (~40 MHz) could also be observed. The sub-splitting into five lines with a characteristic 1:2:3:2:1 intensity pattern is, however, clearly resolved only for two of the ^{59}Co splitted lines (the third and fourth from low field). This super-hyperfine coupling probably originates from the axially bound solvent (here, butyronitrile) molecules. The characteristics of the EPR spectra of **[1-Co]²⁺** and **[2-Co]²⁺** are similar to those of the Co-complexes based on similar ligand systems described by Mulfort and coworkers,[63] wherein the ^{14}N hyperfine splittings have been assigned to two axial MeCN solvent molecules.

The complex **[(bbpya)Co]⁺** with the deprotonated ligand was similarly obtained by reacting equimolar amounts of $Co^{II}(OTf)_2$ and bbpya in dry MeCN for 4 hrs (see SI for detailed synthetic procedure, Figures S15-S16 for characterization). Filtration of the resulting solution followed by vapor diffusion of Et_2O into the filtrate at -25 °C yielded dark orange, needle shaped crystals of

Table 1. Comparison of Bond Lengths in [1-Co]²⁺, [(bbpya)Co]⁺, and [2-Co]²⁺ from Their Molecular Structures (Figure 1)[a] and DFT Calculations.[b]

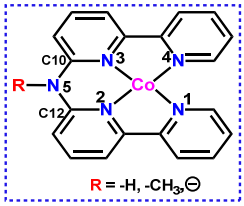

		[1-Co]²⁺	[(bbpya)Co]⁺	[2-Co]²⁺
Co-N1	XRD	1.968(1)	1.964(6)	1.980(1)
	DFT	1.955	1.924	1.988
Co-N2	XRD	1.924(1)	1.889(6)	1.916(1)
	DFT	1.911	1.897	1.937
Co-N3	XRD	1.921(1)	1.905(6)	1.928(1)
	DFT	1.914	1.893	1.928
Co-N4	XRD	1.974(1)	1.937(6)	1.960(1)
	DFT	1.935	1.951	1.962
Co-N5	XRD	3.219(1)	3.273(3)	3.202(1)
	DFT	3.193	3.267	3.191
C12-N5	XRD	1.372(2)	1.348(9)	1.394(2)
	DFT	1.377	1.340	1.390
C10-N5	XRD	1.375(2)	1.324(9)	1.392(2)
	DFT	1.377	1.346	1.397

[a]all bond lengths given in Å, [b] using the BP86 functional.

Table 2. Comparison of the *g* and Hyperfine Tensors for the Cobalt Complexes [1-Co]$^{2+}$, [2-Co]$^{2+}$, and Their Doubly Reduced Analogues from Least-square Fits of the Spectral Simulations and DFT Computations.[c]

Complex		*g*-values	|A|, /MHz
[1-Co]$^{2+}$	Exp. DFT	[2.254, 2.220, 2.026] [2.120, 2.090, 2.008]	27, 91, 249[a] 35, 42, 221
[2-Co]$^{2+}$	Exp. DFT	[2.271, 2.215, 2.025] [2.127, 2.093, 2.008]	36, 63, 258[a] 31, 58, 223
[1-Co]^{0}	Exp. DFT	[2.007, 2.003, 1.971] [2.007,1.998, 1.987]	0,43,18 and 0,28,43[b] SI (Table S12)
[2-Co]^{0}	Exp. DFT	[2.014,1.988, 1.978] [2.007, 2.000, 1.989]	n.a.

[a] hyperfine coupling for the ^{59}Co nucleus,[b] hyperfine coupling for two inequivalent ^{14}N nuclei, [c] using the BP86 functional.

[(bbpya)Co]$^{+}$ suitable for X-ray analysis (Figure 1B). The solid-state structure of **[(bbpya)Co]$^{+}$** reveals a distorted square pyramidal geometry around the cobalt center, with four N atoms from the bipyridine moieties coordinated equatorially at an average Co-N distance of 1.924(3)Å, indicating slightly shortened Co-N distances compared to **[1-Co]$^{2+}$** and **[2-Co]$^{2+}$** (Table 1). One of the two axial coordination sites of Co is occupied by MeCN. Only one counter anion was observed in the X-ray structure, supporting a Co(II) oxidation state and an overall singly charged complex, with a deprotonated amine moiety in the ligand framework. The torsion angle (N1-N2-N3-N4) for **[(bbpya)Co]$^{+}$** is 12.91^{o} , which is slightly larger compared to **[1-Co]$^{2+}$** (Figure S11). The X-band EPR spectrum of **[(bbpya)Co]$^{+}$** in frozen butyronitrile at 14K also exhibited a signal characteristic of low spin Co(II) with well resolved ^{59}Co hyperfine splitting (Figure 2B) along the z direction. The perpendicular components of the spectrum are slightly more broadened in comparison to those of **[1-Co]$^{2+}$** and **[2-Co]$^{2+}$**. Simulation of the spectrum afforded the *g* components [g_x, g_y, g_z] = [2.301, 2.226, 2.017], thus slightly larger in the perpendicular direction in comparison to **[1-Co]$^{2+}$** and **[2-Co]$^{2+}$**. The ^{59}Co hyperfine tensor [A_x, A_y, A_z] = [27, 91, 249] MHz features the largest A_z component of the three complexes.

Synthesis and Characterization of the Reduced Complexes

[1-Co]$^{2+/+/0}$ and [(bbpya)Co]$^{+/0/-}$ Series: The black and red traces in Figure 3 represent the cyclic voltammograms of **[1-Co]$^{2+}$** in MeCN solution containing 0.1 M [N(n-Bu)$_4$]PF$_6$ as the supporting electrolyte in a standard three-electrode set-up consisting of a glassy carbon(GC) working electrode,

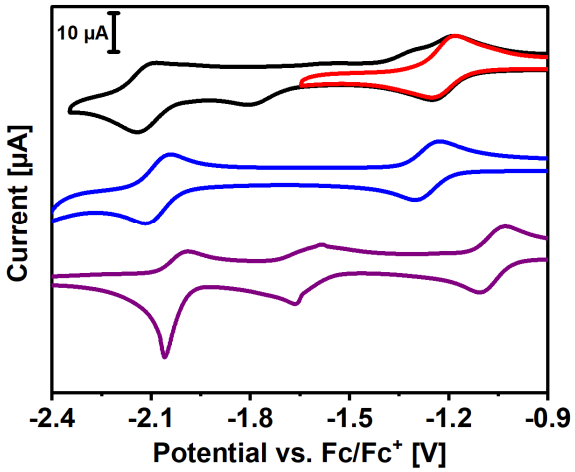

Figure 3. CV data of 0.5 mM solutions of **[1-Co]$^{2+}$** (black trace), **[(bbpya)Co]$^{+}$**, (blue trace) and **[2-Co]$^{2+}$** (purple trace) under Ar in dry MeCN with 0.1 M TBAPF$_6$ at a scan rate of 100 mV s^{-1}. The red trace shows the CV of **[1-Co]$^{2+}$** when scanned up to -1.65V.

a Ag/AgNO$_3$ reference electrode and a Pt-wire as counter electrode. Ferrocene is used as an internal standard, and potentials are referenced against the ferrocenium/ferrocene couple (Fc^{+}/Fc). Complex **[1-Co]$^{2+}$** features a reversible one-electron reduction at $E_{1/2}$ = -1.21 V and two partially reversible reduction processes at E_{red} = -1.78 V and -2.10 V (Figure S17A-F). We assign the first reduction as cobalt centred and the second and third reductions as ligand centred (Scheme 2) based on the comparison of the CV of **[1-Co]$^{2+}$** with the corresponding Zn(II) complex (Table 3, Figure S18A, Figure S19-S20, Figure S21A, and Table S3). This is also supported by

Table 3. Comparison of the $E_{1/2}$ Values for the Redox Processes of [1-Co]$^{2+}$, [(bbpya)Co]$^{+}$, [2-Co]$^{2+}$, and the Corresponding Zn(II) Complexes.[a,b]

Complex	Co$^{2+/+}$	L/L$^{\bullet-}$	L$^{\bullet-}$/L^{2-}
[1-Co]$^{2+}$	−1.21	−1.78(red)[c]	−2.11[d]
[2-Co]$^{2+}$	−1.06	−1.63	−2.02
[(bbpya)Co]$^{+}$	−1.27	−2.08[d]	–
[1-Zn]$^{2+}$	–	−1.71(red)[c]	−1.84(red)[c]
[2-Zn]$^{2+}$	–	−1.64	−1.82
[(bbpya)Zn]$^{+}$	–	−1.85	−2.12

[a]all values given in V vs. Fc/Fc^{+}, [b] for the redox couples within a potential window of −0.8 V to −2.5 V, [c] as these redox features are irreversible, only the potential of the reduction peak is given, [d] reduction of the bbpya ligand.

chemical generation of the reduced species in organic solvents, and their characterizations by UV-Vis absorption, EPR and where possible, by X-ray diffraction studies (Figure S21A, Table S3). The UV-Vis spectrum of **[1-Co]$^{2+}$** in MeCN displays a series of electronic transitions at 228 nm, 253

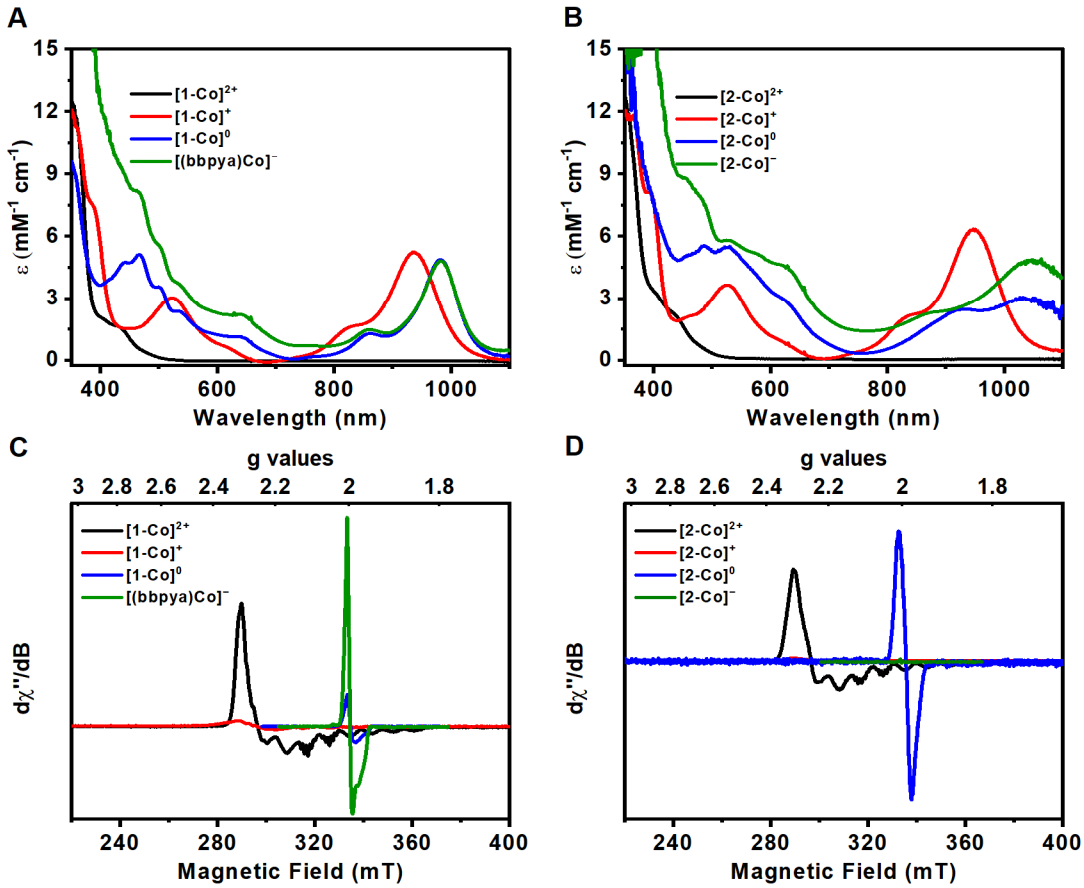

Figure 4. (A) Comparison of the UV-Vis spectra of 0.25 mM **[1-Co]²⁺**(black) with chemically generated **[1-Co]⁺**(red), **[1-Co]⁰** (blue), and **[(bbpya)Co]⁻** (green) in MeCN at 25 °C. (B) UV-Vis spectra of 0.25mM **[2-Co]²⁺**(black), and chemically generated **[2-Co]⁺** (red), **[2-Co]⁰** (blue) and **[2-Co]⁻** (green) in MeCN at 25 °C. (C) Comparison of the X-band EPR spectra of **[1-Co]²⁺** (black)with those of the chemically generated **[1-Co]⁺** (red), **[1-Co]⁰** (blue)[a], and **[(bbpya)Co]⁻** (green) complexes in frozen butyronitrile solution. (D) Comparison of the X-band EPR spectra of **[2-Co]²⁺**(black), with that of the chemically generated **[2-Co]⁺** (red), **[2-Co]⁰** (blue), and **[2-Co]⁻** (green) complexes in frozen butyronitrile solution. EPR conditions: concentration 1mM, microwave frequency ~9.367 GHz, microwave power 0.016mW, modulation amplitude 0.5 mT. All optimized spin-Hamiltonian parameters are listed in Table 2.[a] conditions for this measurement are reported in Figure S26.

nm, 281 nm, 328 nm, 346 nm, and a shoulder around 434 nm (Figure 4A, black trace, Figure S22). These bands are tentatively assigned to the π to π* transitions associated with the bipyridine moieties in the ligand framework and metal to ligand charge transfer (MLCT) transitions consistent with previous observations for complexes containing polypyridine ligands.[62, 64] One electron reduction of **[1-Co]²⁺** to form **[1-Co]⁺** by the addition of one equivalent reductant (decamethylcobaltocene, $CoCp_2^*$) leads to the appearance of characteristic new transitions in the near-infrared (NIR) region at 827 nm and 937 nm (Figure 4A, red trace). **[1-Co]⁺** can also be generated by electrochemical reduction of **[1-Co]²⁺** at -1.36 V (Figure S23). The NIR bands are red-shifted to 849 and 968 nm in **[1-Co]⁰** (Figure 4A, blue trace), which is generated by addition of two equivalents of $CoCp_2^*$ to **[1-Co]²⁺** or electrochemical reduction at -1.8V (Figure S24). Further reduction of **[1-Co]²⁺** by three equivalents of reductant leads to an increase in intensity of the bands near the UV region (Figure 4A, green trace). As mentioned before, the X-band EPR spectrum of **[1-Co]²⁺** revealed a low spin Co(II) signal (Figure 2A) with g tensors $[g_x, g_y, g_z]$ = [2.254, 2.220, 2.026]. **[1-Co]⁺**, in contrast, is EPR silent consistent with a low spin Co(I) assignment (Figure 4C, red trace, Figure S25). The EPR spectrum of **[1-Co]⁰** at 14K revealed a signal that is diagnostic of a ligand radical centred around g_{av}=1.993 and extending over 15 mT (Figure 4C, blue trace). The simulation of the spectrum revealed a slightly rhombic g tensor with principal components $[g_x, g_y, g_z]$ = [2.003, 2.007,1.971], and hyperfine interactions arising from two inequivalent nitrogen atoms, supposedly of the pyridinyl moeities, which exhibit different spatial orientations, with hyperfine tensors of [0, 43, 18] MHz and [0, 28, 43] MHz, respectively (Figure 5A). Spin quantifications (Figure S26) revealed that the S = 1/2 EPR signal of **[1-Co]⁰** accounts for only 10% of the initial Co(II)-spins, as represented by the **[1-Co]²⁺** spins, thus implying that **[1-Co]⁰** is metastable, and that a majority of it decays to an EPR silent species. The nature of this species could be established by chemical reduction of **[1-Co]²⁺** by two equivalents of $CoCp_2^*$ in MeCN.

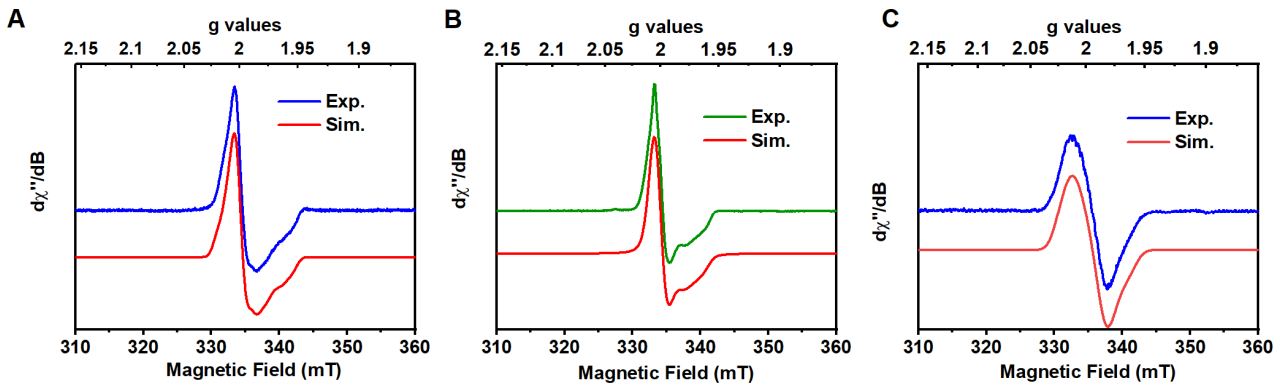

Figure 5. X-band EPR spectra of (A) **[1-Co]^{0}** (experimental: blue and simulation: red), (B) **[(bbpya)Co]$^{-1}$** (experimental: green and simulation: red) and (C) **[2-Co]^{0}** (experimental: blue and simulation: red) respectively. The following parameters were used for the simulations: (A) g_x = 2.007, g_y = 2.003, g_z = 1.971 , lwpp = [1.97 0.96] , |A_N |, /MHz= 0, 42, 18 , |$A_{N'}$|, /MHz= 0, 28, 43. (B) g_x = 2.002, g_y = g_z = 1.970, lwpp = 1.88 , |A_N |, /MHz= 0, 6, 36. (C) g_x = 2.014, g_y = 1.988, g_z = 1.978, lwpp = [2.44 0.42] , anisotropic broadenings (in MHz): HStrain(1) = 0 , HStrain(2) = 38 , Hstrain(3) = 134.

Single crystals suitable for X-ray diffraction studies were obtained by vapor diffusion of Et_2O into a tetrahydrofuran (THF) solution. The solid-state structure revealed the formation of a neutral **[(bbpya)Co^{I}]^{0}** (Figure 1D) species comprising the deprotonated Hbbpya ligand. The bbpya ligand surrounds the cobalt(I) ion with a torsion angle (N1-N2-N3-N4) of 15.69 ° (Figure S11D), which is slightly larger than that in **[(bbpya)Co^{II}]$^{+}$** (12.91 ° ,Figure S11C). Intriguingly, the average Co-N distance in **[(bbpya)Co^{I}]^{0}** of 1.877(5) Å (Table S4) is significantly shorter than the average Co-N distance in **[(bbpya)Co]$^{+}$** (1.924(3) Å), hence, establishing a stronger metal-to-ligand back donation from the electron rich Co(I) center. Electrochemical generation of **[1-Co]^{0}** by electrolysis at -1.8 V also leads to the decay of **[1-Co]^{0}**, as evident from the low-yield (~10%) generation of **[1-Co]^{0}** (Figure S25, green trace), as obtained from EPR spectroscopy. The conversion of S = 1/2 **[1-Co]^{0}** to the EPR silent S = 0 **[(bbpya)Co^{I}]^{0}** species is associated with the stoichiometric release of hydrogen (Scheme 2A), which was detected by gas-chromatography (Figure S27). This dehydrogenation step is an inherent property of the reduced Hbbpya ligand. Accordingly, the corresponding [(Hbbpya)Zn^{II}]$^{2+}$ (**[1-Zn]$^{2+}$**) complex undergoes a similar dehydrogenation step to yield **[(bbpya)Zn^{II}]$^{+}$**, as evident from X-ray diffraction, NMR, and EPR studies (Scheme S4 , Figures S28-S30). The complex **[(bbpya)Co^{I}]^{0}** can be further reduced by one electron to **[(bbpya$^{\bullet-}$)Co^{I}]$^{-}$**, which exhibits a S = 1/2 signal with g_{av} = 1.980 and a width of 14.3mT, indicating that the unpaired electron resides in a ligand centred orbital (Figure 4C, green trace). The best simulation result was achieved with a slightly axial g tensor [$g_{\perp}$, $g_{\parallel}$] = [2.002, 1.970] and only one ^{14}N hyperfine interaction prevalent along the parallel direction with a coupling constant A_z of 36 MHz (Figure 5B), supposedly also representing pyridyl nitrogen(s). The **[(bbpya$^{\bullet-}$)Co^{I}]$^{-}$** complex is also accessible by two electron reduction of **[(bbpya)Co^{II}]$^{+}$**, as corroborated by the presence of two reduction processes in the CV (see Figure 3, blue trace, Scheme 2, and Figure S31).

[2-Co]$^{2+/+/0/-}$ Series: The CV of **[2-Co]$^{2+}$** (Figure 3, purple trace) shows three reversible redox couples at -1.06 V, -1.63 V and at -2.02 V (Figure S32). These values are consistent with those of a previously reported cobalt complex of a similar ligand system with a -N(C_4H_9) bridge between the two bpy units instead of -N(CH_3), as detailed by Mulfort and co-workers. [61,63] Notably, all three redox couples are slightly shifted anodically in comparison to **[1-Co]$^{2+}$** (Table 3). Again, based on comparison to the corresponding Zn(II) complex (Figure S18B, Figure S21B, Figures S33-S35, Table S3), we assign the first reduction event at -1.06 V as a metal centred process, while the subsequent events likely pertain to ligand centred processes (Scheme 2). One electron reduction of **[2-Co]$^{2+}$** also leads to the appearance of near-IR bands in the UV-Vis absorption spectrum (Figure 4B, red trace); the bands in EPR silent (Figure 4D, red trace) **[2-Co]$^{+}$** are observed at 832 and 945 nm, which are significantly red shifted compared to **[1-Co]$^{+}$**. Single crystals of X-ray quality were obtained by slow evaporation of a propionitrile solution of **[2-Co]$^{+}$**. The X-ray diffraction analysis revealed that **[2-Co]$^{+}$** has a distorted square planar geometry (Figure 1E). The average Co-N distance in **[2-Co]$^{+}$** is 1.887(7) Å , which is significantly shorter than that in **[2-Co]$^{2+}$** (1.946(1) Å), stressing a stronger Co(I) to ligand back-bonding interaction in **[2-Co]$^{+}$.** Further reduction leads to the generation of **[2-Co]^{0}**, where the near-IR absorption features are red shifted to 942 and 1035 nm (Figure 4B, blue trace), respectively. **[2-Co]^{0}** is an EPR active species, as expected, exhibiting a ligand based radical signal (Figure 4D, blue trace), which is centred around g_{av} = 1.993, extends over 20 mT, and is more rhombic in comparison to **[1-Co]^{0}**. The principal g components for **[2-Co]^{0}** were determined as [g_x, g_y, g_z] = [2.014, 1.988, 1.978] from simulation (Figure 5C, Table 2). While no hyperfine splitting structure is resolved in the signal, residual hyperfine couplings from the ^{59}Co and/or ^{14}N centres likely contribute to its linewidth, which has been accounted for in the simulation by an anisotropic broadening. Complex **[2-Co]^{0}** could be further reduced by one electron

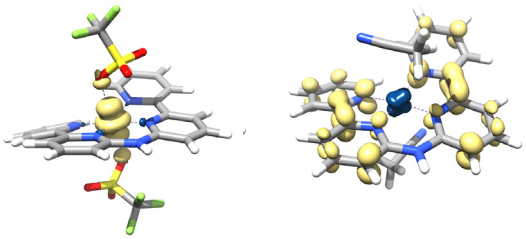

Figure 6. Spin density plots at an isovalue of 0.003 as obtained from DFT at the BP86 level for (left) **[1-Co]²⁺**, where the unpaired electron is located in a dz^2-type orbital; (right) **[1-Co]⁺** where a low-spin Co(I) center is ligated to a single unpaired electron delocalized over the entire ligand .

to generate **[2-Co]⁻**, which is EPR silent (Figure 4D, green trace).

Electronic Structure Calculations

To aid the interpretation of the experimental results and verify their implications for the electronic structure of [**1-Co**] and its derivatives, we have conducted a series of electronic structure calculations on the DFT level of theory. Prior to any discussion of our results, we would like to point out that all electronic states that feature antiferromagnetically coupled electron spins, were described within the BS-DFT formalism. In agreement with the X-band EPR results, various density functionals of GGA (BP86) and hybrid type (TPSSh and B3LYP) predict a low-spin Co(II) center with total spin of $S = 1/2$ for **[1-Co]²⁺**. The spin density shown in Figure. 6A reveals that the unpaired electron is located in a d_{z^2} -type orbital of the Co center and the computed g values of 2.120, 2.090 and 2.007 (BP86) reproduce the experimentally observed values well (Table 2, Table S7). For the one-electron reduced species **[1-Co]⁺**, the GGA functional BP86 converges to a Co(I) low-spin state ($S = 0$), which is consistent with the experiment. However, the other tested density functionals lead to a different electronic ground state with a low-spin Co(II) center whose spin is antiferromagnetically coupled to a ligand radical (Figure 6; left). Our somewhat mixed findings demonstrate the complicated character of the electronic structure in **[1-Co]⁺**. Accordingly, initial studies with multireference (MR) electronic structure methods indicate that the electronic ground state of **[1-Co]⁺** is multiconfigurational in nature which has previously been observed for other cobalt complexes with redox non-innocent ligands.[67-68] In fact the NIR features at 827 nm and 937 nm in the absorption spectrum, which presumably originate from a Co(I) to ligand charge transfer transition in **[1-Co]⁺**, corroborate that the Co(II)-ligand radical state is indeed close in energy relative to the ground low-spin Co(I) configuration (Table S5). Upon a second reduction process, **[1-Co]⁰** is formed. For this species, BP86 predicts a low-spin Co(I) ground state that features a single unpaired electron delocalized over the entire ligand (see Figure 6, right). Comparison of the BP86 computed g values of 2.007, 1.998, 1.987 with their experimental counterparts (Table 2) indicates that this state is realistic (Table S7). Furthermore, our computational results indicate that the electronic ground states of **[2-Co]²⁺/⁺/⁰** have the same general character as the corresponding **[1-Co]²⁺/⁺/⁰** complexes (Table S8-S9).

Electrocatalytic Reduction of CO_2 Catalyzed by [1-Co]²⁺ and [2-Co]²⁺ in MeCN.

In spite of their similar electronic structures, **[1-Co]²⁺** and **[2-Co]²⁺** exhibit different reactivities and product selectivity towards electrocatalytic CO_2 reduction reactions. The different CO_2RR abilities are reflected in the CVs of **[1-Co]²⁺** and **[2-Co]²⁺** in the presence of CO_2 (Figure 7). In **[1-Co]²⁺** (Figure 7A) the first two redox processes become irreversible and undergo a cathodic shift relative to the CV under argon. The most cathodic redox couple also becomes completely irreversible; however, it is anodically shifted with a 4-fold enhancement of peak intensity, even in the absence of any added external proton source. The CV of **[2-Co]²⁺**, in contrast, is less affected by the presence of CO_2 (Figure 7B). For **[1-Co]²⁺**, addition of a proton source in a CO_2 saturated MeCN solution triggers the emergence of significant catalytic current with an onset potential of about -1.65 V (corresponding to the **[1-Co]⁺/[1-Co]⁰** couple), reaching a maximum at -2.1 V (Figure 7C). The current increases with increasing phenol concentration and reaches a plateau with 2.5M phenol concentration (Figure S36). This increase in current could be attributed to enhanced CO_2 reduction activity of **[1-Co]²⁺** in the presence of an acid source (3M phenol) with a $\frac{i_{cat}}{i_p} \approx 28$. Incidentally, the first reduction event remains nearly unchanged (Figure 7C, inset), thereby establishing **[1-Co]⁰** as the reactive intermediate responsible for CO_2RR activity. For **[2-Co]²⁺**, a similar increase in activity (i_{cat}/i_p) and positive shifts in the onset potential could be observed in the presence of both

CO_2 and phenol (Figure 7D), but the magnitude of the catalytic current is significantly smaller ($\frac{i_{cat}}{i_p} \approx 10$) relative to **[1-Co]²⁺** when recorded at the same scan rate. These findings suggest that **[2-Co]²⁺** is less effective in promoting CO_2 reduction in the presence of phenol, highlighting the importance of the secondary coordination sphere (-NH vs -NCH_3 in **[1-Co]²⁺** and **[2-Co]²⁺**, respectively) in modulating the CO_2RR activity.

Controlled Potential Electrolysis (CPE) Studies for Direct Product Measurements of Electrochemical CO_2RR Catalyzed by [1-Co]²⁺ and [2-Co]²⁺.

To verify our findings regarding the trends of CO_2RR activity of **[1-Co]²⁺** and **[2-Co]²⁺** from CV experiments, chronopotentiometry was conducted over 8h using a 0.5 mM complex solution in MeCN with 3 M PhOH as a proton source at a constant CO_2 pressure (1 atm). The gaseous products were analysed in two-hour intervals for the entire 8h period by injection into a gas chromatograph with barrier discharge ionization detector (GC-BID).

At a potential of -1.8 V, **[1-Co]²⁺** shows a faradaic efficiency (FE) of 79% for CO and only 2% for H_2 after 2h of electrolysis (Figure8, Table 4). Over the 8 h of catalysis, the FE_{H2} slightly increases up to 7%, while the FE_{CO} remained stable at 75% with a selectivity of 95 % for CO. The high selectivity for CO production and the overall FE are also maintained in the corresponding deprotonated complex, **[(bbpya)Co]⁺** (Table 4) over 8h. Bulk-electrolysis at a potential of -1.68 V, which is slightly more positive compared to **[1-Co]²⁺**, again produced CO nearly as the sole product with a FE of ≥ 90%. The whole 8 hours of catalysis produced only negligible amounts of H_2 (FE of <2%). The replacement of the -NH group in **[1-Co]²⁺** by-NCH_3 in **[2-Co]²⁺**, however, led to a significant decrease in selectivity for CO production and also in the overall activity (CO+H_2 production all together). After 2 h of electrocatalysis by **[2-Co]²⁺** at -1.75 V, FEs of 40% and 26% are detected for CO and H_2, respectively. The extent of HER increases with time and H_2 becomes the predominant product (over 60 % selectivity

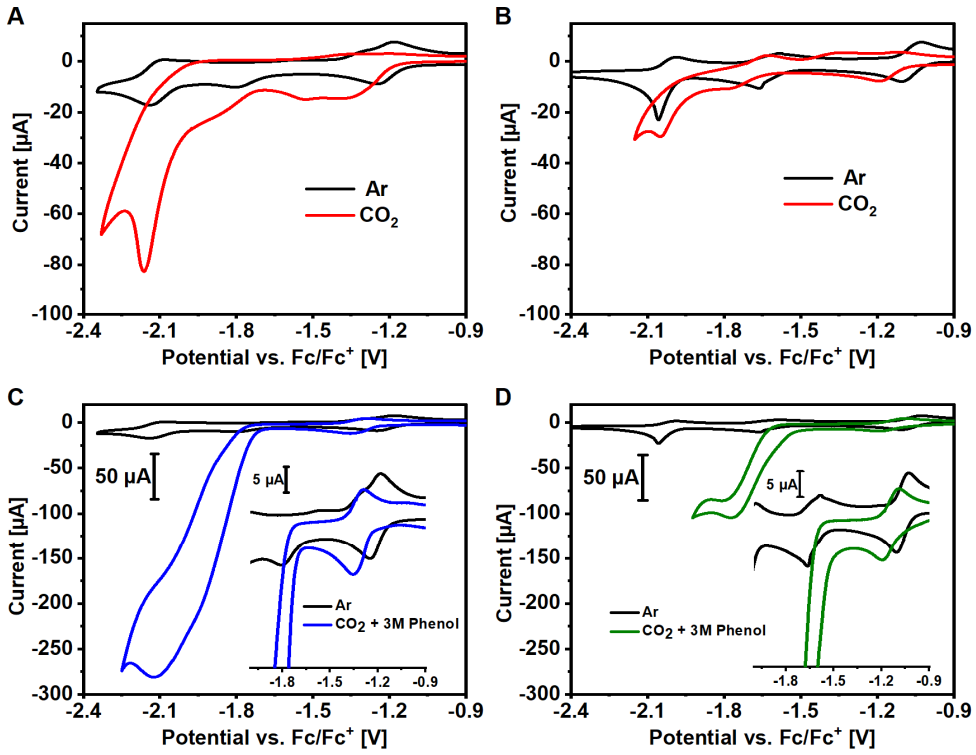

Figure 7. CVs of 0.5 mM Ar (black) and CO_2 saturated (red) MeCN solutions of (A) **[1-Co]²⁺** and (B) **[2-Co]²⁺** in presence of 0.1M $TBAPF_6$. The corresponding CVs in presence of both CO_2 and 3M phenol as proton source for **[1-Co]²⁺** (blue) and **[2-Co]²⁺** (green) are shown in (C) and (D), respectively. Scans were performed at a scan rate of 100 mVs^{-1}.

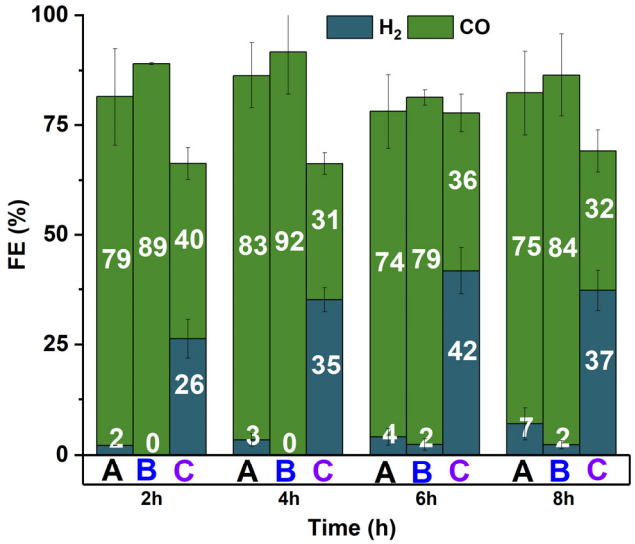

Figure 8. Results of the product analysis of the long-term electrolysis of CO_2 saturated MeCN solutions of **[1-Co]²⁺** (A), **[(bbpya)Co]⁺** (B), and **[2-Co]²⁺** (C) at -1.80 V, -1.69 V and -1.75 V, respectively, in presence of 3 M PhOH.

for H_2 production) between 4 and 8 h of electrocatalysis (Figure 8, Table 4).

Kinetic Analysis of Electrochemical CO_2RR Catalyzed by [1-Co]²⁺ and [2-Co]²⁺.

Encouraged by the high selectivity of **[1-Co]²⁺** for electrochemical CO_2RR, and the change of selectivity for **[2-Co]²⁺** towards competing HER we sought to evaluate the kinetic factors leading to the different selectivity in **[1-Co]²⁺** and **[2-Co]²⁺**. Accordingly, CV studies were conducted using increasing phenol and phenol-d⁶ concentrations (0.5 M–3 M) (Figure S36-S37). The catalytic current increased linearly with increasing H^+/D^+ concentrations, and plateaued at a 2.5 M concentration of PhOH/PhOD. Kinetic isotope effect (KIE) values were determined from the linear plots of (I_{cat}/I_p) with respect to PhOH or PhOD concentrations measured at a scan rate of 0.1 V/s. A KIE value of 1.13 was calculated for **[1-Co]²⁺** (Figure S36), which is consistent with the formation of a [Co-CO_2H] intermediate (Scheme 1), and the involvement of a rate determining hydrogen-bond mediated proton transfer step in the C-OH bond cleavage process to yield CO.[18, 69-70] Interestingly, a significantly higher KIE of 7.73 was determined for **[2-Co]²⁺**(Figure S37), which suggests the generation of a Co-H intermediate (Scheme 1), instead.[44, 71-72] Co-H can react either with a proton to produce H_2 or with CO_2 to generate formate (HCO_2^-; Scheme 1). The selectivity between H_2 and HCO_2^- largely depends on the hydricity of the generated Co-H and the pK_a of the proton donor during catalysis.[47] A hydricity of 42.42 kcal mol^{-1} (see SI) has been determined for the cobalt-hydride species generated in the reaction of **[2-Co]⁰** and H^+ using the empirical equation developed by Kubiak et al.[45] and the experimentally determined reduction potential ($E_{1/2}$) for the catalytically relevant **[2-Co]⁺/⁰** couple. Based on the thermodynamic product diagram describing metal hydride reactivity with protons and CO_2 in acetonitrile,[45, 47] **[2-Co]²⁺** operates in a zone where H_2 evolution is energetically much more favourable in comparison to the generation of HCO_2H (see SI for details). For the preferential generation of HCO_2H at the pK_a of the experimental condition, the hydricity value of the corresponding metal hydride has to be below 40 kcal mol^{-1}.[45-46] This explains why no HCO_2H is detected during electrocatalytic CO_2RR mediated by **[2-Co]²⁺**.

Table 4. Quantification of the Gaseous Products During CPE of [1-Co]²⁺, [(bbpya)Co]⁺ and [2-Co]²⁺[a,b]

Complex	Eapp/ V	Time /h	FE /%		Q /C	Selectivity (CO), /%	TON (CO)[c]
			H_2	CO			
[1-Co]²⁺	−1.8	2	2	79	2.9	95	52
		4	3	83	5.4		
		6	4	74	7.1		
		8	7	75	8.4		
[(bbpya)Co]⁺	−1.69	2	0	89	0.9	92	22
		4	0	92	1.9		
		6	2	79	3.1		
		8	2	84	4.5		
[2-Co]²⁺	−1.75	2	26	40	1.5	40	5
		4	35	31	2.2		
		6	42	36	2.6		
		8	37	32	3.0		

[a] Conditions: 0.5mM complexes in CO_2 saturated MeCN with 3 M phenol as proton source, [b]reported values are averages from three or more independent measurements, [c]TON is given after 8 h of electrolysis, TON has been calculated from the total amount of product formed (CO) after 8 h of electrolysis with respect to catalyst concentration.

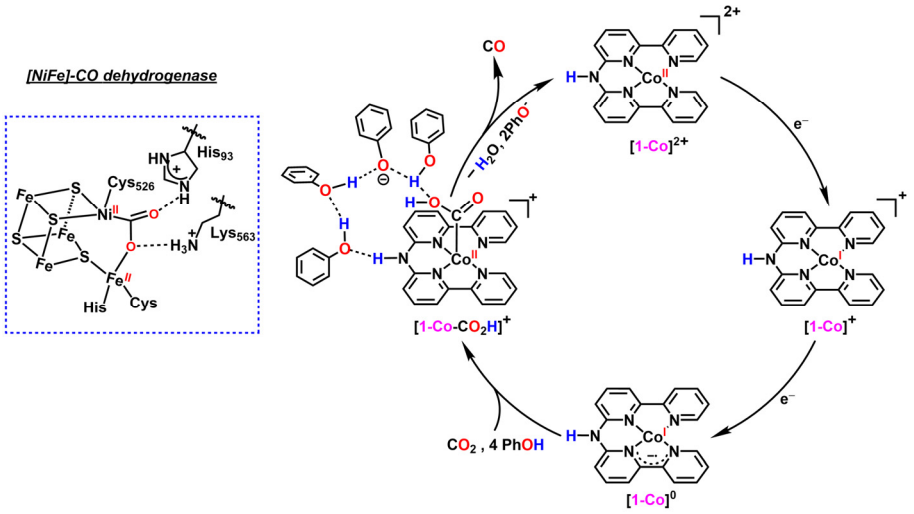

Figure 9. (Right) Proposed reaction mechanism for CO_2 reduction by **[1-Co]²⁺** in the presence of 3 M phenol; (Left) Proposed intermediate stabilised by H bonding from second-sphere histidine and lysin residues during CO_2 activation by the [NiFe]-CODH enzyme.

Stoichiometric Reactions of [1-Co]⁰ and [2-Co]⁰ with H⁺ and CO_2.

The conclusions derived from the kinetic analysis of electrocatalytic CO_2RR are also supported by the kinetics of the stochiometric reactions of CO_2 and PhOH with chemically generated doubly reduced **[1-Co]⁰** and **[2-Co]⁰** complexes. Notably, reaction of **[1-Co]⁰** with CO_2 at room temperature led to the stoichiometric formation of CO with the concomitant formation of the two electron-oxidized **[1-Co]²⁺** species, as evidenced by EPR and UV-Vis studies (Figures S38-S39). Reaction of the in-situ generated **[1-Co]⁰** with CO_2 saturated acetonitrile (0.28M CO_2)[73] was monitored by UV-Vis spectroscopy, and the kinetics were evaluated by monitoring the decay of the characteristic NIR band of **[1-Co]⁰** at 968 nm over time at -10°C (Figure S40A). The decay of the band follows a first-order kinetics, for which a pseudo-first-order rate constant of 0.197 s^{-1} was determined (Figure S40B). **[1-Co]⁰** also decays in presence of H^+ (0.28M PhOH) to form first the one-electron oxidized **[1-Co]⁺** species, which then decays at a rate 54 times slower (Figure S41) than that obtained for CO_2. In **[2-Co]⁰** the reactivity trend is reversed; a much faster reaction with H^+ is observed leading to the stoichiometric formation of H_2 (Figure S42). Furthermore, in contrast to **[1-Co]⁰**, which acts as a two- electron reductant for CO_2, **[2-Co]⁰** can only transfer one-electron to CO_2 forming the one-electron oxidized **[2-Co]⁺** species, as evident from the immediate generation of the UV-Vis band at 945nm corresponding to **[2-Co]⁺**, in the reaction of **[2-Co]⁰** with CO_2 (Figure S43). We envisage, that an efficient proton coupled electron transfer in the transient **[1-Co^{I}-$CO_2^{\bullet-}$]** in presence of the -NH bridge in the Hbbpya ligand leads to barrier less generation of **[1-Co^{II}-CO_2H]**, which then undergoes spontaneous C-OH bond cleavage to form CO and **[1-Co]²⁺**. This is also supported by our theoretical calculations (see below). For the corresponding complex involving the Mebbpya ligand, in contrast, the protonation step is much slower, so that the **[2-Co^{I}-$CO_2^{\bullet-}$]** species has sufficient life-time to decay to **[2-Co]⁺** and presumably C-C coupled products. Indeed, oxalate is detected in the reaction in 10% yield. This also explains the significantly lower FE of **[2-Co]²⁺** for CO and H_2 production compared to **[1-Co]²⁺**(Figure 8, Table 4).

Proposed Mechanism Supported by DFT Calculations.

Based on these findings, a reaction mechanism can be proposed for catalytic CO_2 reduction by **[1-Co]²⁺** in the presence of phenol as an acid source (Figure 9). The starting **[1-Co]²⁺** must initially undergo a two-electron reduction process to form **[1-Co]⁰**. In the absence of any substrate (proton/CO_2) the ligand undergoes a dehydrogenation process to generate **[(bbpya)Co]⁰** (Scheme 2). The calculated thermodynamic Gibbs free energy of -8.35 kcal mol^{-1} using BP86 functional agrees with the spontaneous dehydrogenation process from **[1-Co]⁰** (Table S14). Our DFT calculations show that the -NH group in **[1-Co]⁰** interacts via a hydrogen bond to a phenol moiety and thereby acts as a structural anchor to organise further phenol molecules that form a hydrogen bonded network. This network efficiently stabilizes **[1-Co]⁰** and prevents a dehydrogenation reaction. Moreover, the phenol network facilitates the binding of CO_2 to the Co center in **[1-Co]⁰**. When four phenol molecules are assembled in the hydrogen bonded network and a CO_2 molecule approaches the Co center, formation of **[1-Co-CO_2]** is exergonic by ΔG = -4.1 kcal mol^{-1}. Interestingly, our simulations indicate that formation of a hydrogen bond to one of the adjacent phenols adds substantially to the negative free energy of this step (see Figure 10). In **[1-Co-CO_2]** the bound substrate interacts via hydrogen bond with one of the present phenol molecules. The same phenol can readily transfer its proton to the carboxylate group and the resulting phenolate is then stabilized by three neighbouring phenol molecules, one of which is polarized by a hydrogen bond to the NH group of the Hbbpya ligand.

When less than four phenol molecules are involved, the protonation of **[1-Co-CO_2]** is less feasible. If only a single phenol acts as proton source the reaction is predicted to be endergonic by ΔG = +5.2 kcal mol^{-1} At this point it should be noted that in **[1-Co-CO_2]**, a direct interaction between the NH moiety of the ligand and the bound CO_2 substrate is

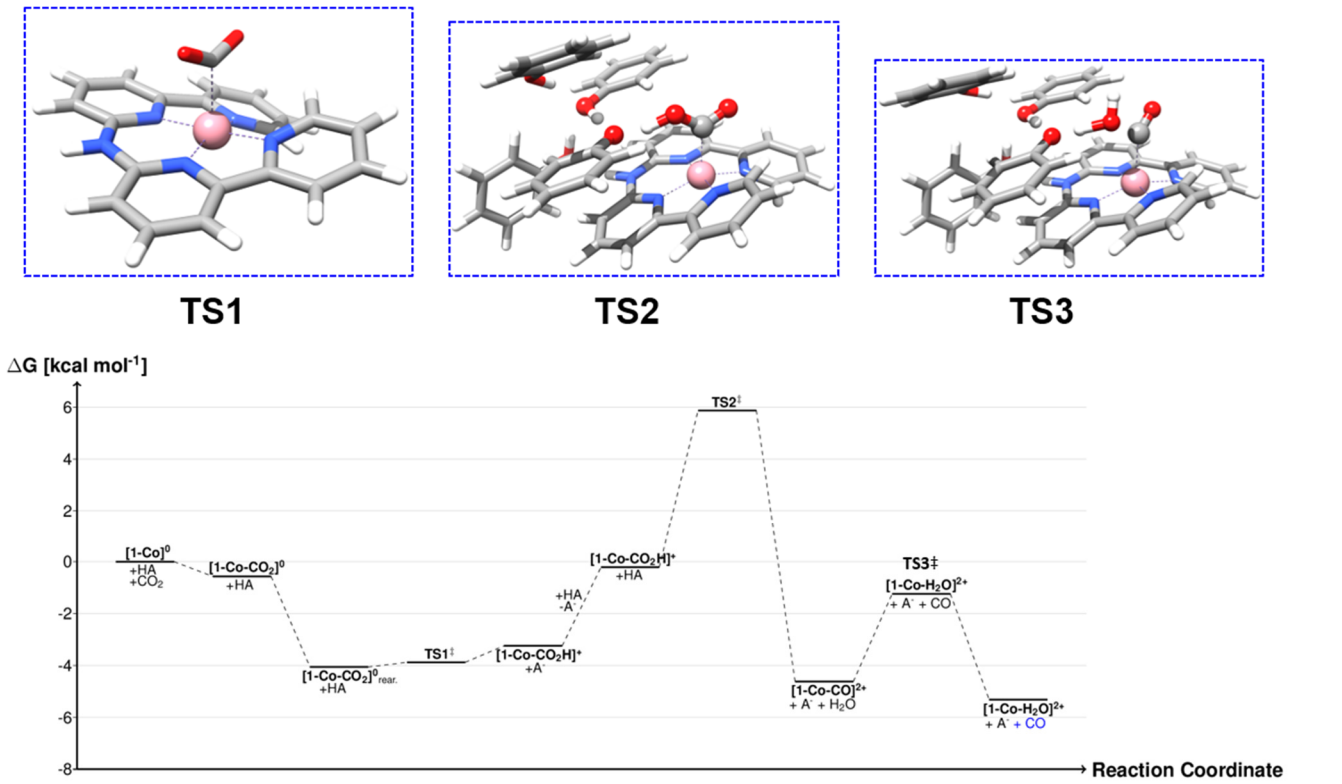

Figure 10. Free energy profile of CO_2 reduction by **[1-Co]⁰** as obtained from DFT calculations (Tables S15-S17). TS1 corresponds to a transition state on the electronic PES but subtle differences in the thermochemical corrections its free energy is lower than **[1-Co-CO₂H]**. The CO highlighted in blue indicates that the CO molecule has been computed separately leading to a considerable gain in translational entropy. AH is a cluster of 4 phenol molecules while A- is a cluster of 3 phenols with one phenolate.

impossible on account of their large spatial separation of 4.13 Å and the unfavorable N-H-O angle of 39.8 °. Analogous to its effect on substrate binding, loss of the phenol network also impedes the subsequent protonation of **[1-Co-CO₂]**. If only a single phenol acts as proton source the reaction is predicted to be endergonic by ΔG = +5.2 kcal mol^{-1}. In **[2-Co]⁰**, owing to the absence of any anchor for a H-bonded phenol network, presumably both CO_2 and H^+ compete for binding to the Co center, leading to the observed loss of selectivity (see Scheme S5 for the proposed mechanism). Notably, proton transfer chains as the one proposed here are well known and excessively studied in water networks.[74-75] At this point we would like to emphasize that our results rather provide a "proof of principle" for the sequential proton transfer, stabilization of the phenolate and the involvement of the NH moiety as an external polarizer and directing group. Of course, larger networks of phenols as well as networks that also involve water molecules (which are progressively formed during the CO_2 reduction reaction) can facilitate the proton transfer. Moreover, we do not further dive into the intricacies of the dynamics of these proton transfer networks as this is well beyond the scope of this study and not expected to yield information that are relevant in this context. After one proton is transferred, we assume that the phenol group is readily recharged by either the excess phenol or water that is being formed during the reaction. The subsequent second protonation step that leads to the formation of **[1-Co-CO]** and water is again facilitated by a phenol mediated proton transfer to the CO_2H group. However, owing to the C – O bond breaking this step is associated with a reaction barrier of $\Delta G^{\ddagger}$ = 6.0 kcal mol^{-1}. TS3 is depicted in Figure 10.

3. CONCLUDING REMARKS

In nature, the enzyme CO-dehydrogenase (CODH) catalyzes the selective and reversible ($2e^- + 2H^+$) conversion of CO_2 to carbon monoxide (CO), whereby efficient CO_2 reduction and protonation at a binuclear NiFe cluster is mediated by hydrogen bonding interactions from appropriately positioned amino acid residues, as revealed by structural studies of the active site.[5, 76-77] Pendant proton donors also facilitate catalysis of HER in nature, for example hydrogen evolution at the diiron site in FeFe-hydrogenase.[5, 78] These studies have inspired the development of biomimetic CO_2RR and HER catalysts that involve a transition-metal center surrounded by ligands with pendant proton donors.[22, 48, 79-83] For example, in CO_2RR, which is more relevant to the present study, the electrochemical CO_2-to-CO activity of metal complexes was previously shown to increase with the incorporation of pendant phenol or secondary amine moieties into the ligand scaffold. The higher efficiency and product selectivity have been attributed to stabilization of the bound CO_2 by intramolecular hydrogen bonds. In the present report of the electrocatalytic CO_2RR mediated by **[1-Co]²⁺** such a H-bonding of the CO_2 adduct is, however, unavailable; the ring deformation required to position the N–H of the rigid Hbbpya ligand for CO_2 binding comes at a high energetic cost, and is inaccessible under catalytic conditions. The

observed lower catalytic efficiency and selectivity of the methylated analogue, **[2-Co]$^{2+}$**, can rather be explained by the differences in the two protonation steps following CO_2 binding that are necessary for the release of CO. Notably, enhanced currents are observed at potentials near that for the **[1-Co]$^{+/0}$** or **[2-Co]$^{+/0}$** couples upon addition of CO_2, suggesting that **[1-Co]^0** or **[2-Co]^0** can bind the substrate to form [Co(CO_2)] adducts. Stoichiometric and kinetic studies and complementary DFT calculations suggest that the protonation of **[2-Co-CO_2]^0** occurs slowly and sequentially, with the first protonation forming a COOH ligand and the second protonation cleaving the C–OH bond to form water and CO. The direct binding of H^+ to form a Cobalt-hydride species competes with the CO_2 binding to the Co center, as evidenced by the large PhOH/PhOD KIE of 7.73 in the reaction, and formation of both H_2 and CO products. The reaction of **[1-Co]^0** with CO_2, in contrast, leads to the formation of the two-electron oxidation product **[1-Co]$^{2+}$**, with the concomitant release of CO. Thus, the two protonation steps occur very fast in a concerted way from PhOH to CO_2 and mediated by an efficient H-bonded network involving four PhOH moieties and -NH group of the Hbbpya ligand, as corroborated by the relatively lower PhOH/PhOD KIE of 1.13. This also leads to the observed much faster reaction of **[1-Co]^0** with CO_2 relative to H^+, which explains the high CO selectivity in CO_2RR. The CO_2RR mechanism in **[1-Co]$^{2+}$** is, therefore, reminiscent of the proposed two-electron reduction of CO_2 at the Ni(0)Fe(II) center in NiFe-CODH to form Ni^{II}-(CO_2^{2-})Fe^{II}, where the CO_2^{2-} moiety is stabilized by H-bonding interactions involving the protein residues (Figure 9 inset).[77] Notably, in preliminary studies in water, an efficient proton channel is available for both complexes and the difference in selectivity diminishes and both complexes exhibit high TON and TOF. In the absence of any stabilizing H-bonding interaction, one-electron chemistry prevails in the reaction of **[2-Co]^0** and CO_2 to form the high-energy CO_2 radical anion product, which is avoided in biology and in **[1-Co]^0**. CO_2RR mediated by **[1-Co]$^{2+}$**, therefore, provides a relevant model for biological systems, and offers a framework for tuning the effect of the second coordination sphere on CO_2 reduction, and more generally, on multielectron, multiproton reduction reactions.

ASSOCIATED CONTENT

Supporting Information.

The Supporting Information is available free of charge via the Internet at http://pubs.acs.org.

Experimental Section, Synthesis of ligands and complexes, Figure S1-S43 (characterizations of ligands and complexes, additional spectroscopic data, and electrochemistry) Table S1-S17(for detailed crystallographic data and DFT calculations)

AUTHOR INFORMATION

Corresponding Authors

* Kallol Ray – Department of Chemistry, Humboldt-Universität zu Berlin, Brook-Taylor-Str.2, 12489 Berlin; https://orcid.org/0000-0003-2074-8844; Email: kallol.ray@chemie.hu-berlin.de

*Ulf-Peter Apfel – Faculty of Chemistry & Biochemistry, Ruhr-Universität Bochum, Universitätsstraße 150, 44801 Bochum, Germany, Department of Electrosynthesis, Fraunhofer UMSICHT, Osterfelder Straße 3, 46047 Oberhausen, Germany.; https://orcid.org/0000-0002-1577-2420 ; Email: ulf.apfel@rub.de

*Michael Römelt – Department of Chemistry, Humboldt-Universität zu Berlin, Brook-Taylor-Str.2, 12489 Berlin; https://orcid.org/0000-0002-4780-5354; Email: michael.roemelt@hu-berlin.de

Author Contributions

The manuscript was written through contributions of all authors. / All authors have given approval to the final version of the manuscript. / ‡These authors contributed equally.

Funding Sources

This work was funded by the Deutsche Forschungsgemeinschaft (DFG, German Research Foundation) under Germany's Excellence Strategy – EXC 2008-390540038 – UniSysCat and the Heisenberg-Professorship to K.R. U.-P. A. was funded by the Deutsche Forschungsgemeinschaft under Germany's Excellence Strategy, EXC-2033 (Projektnr. 390677874). T. L. received funding by DFG under Project No. LO 2898/1-1. K.A. gratefully acknowledges funding through DFB Center of Exellence 1487.

Notes

Any additional relevant notes should be placed here.

ACKNOWLEDGMENT

(Word Style "TD_Acknowledgments"). Generally the last paragraph of the paper is the place to acknowledge people (dedications), places, and financing (you may state grant numbers and sponsors here). Follow the journal's guidelines on what to include in the Acknowledgement section.

REFERENCES

1. Birdja, Y. Y.; Pérez-Gallent, E.; Figueiredo, M. C.; Göttle, A. J.; Calle-Vallejo, F.; Koper, M. T. M., Advances and challenges in understanding the electrocatalytic conversion of carbon dioxide to fuels. *Nature Energy* **2019,** *4* (9), 732-745.
2. Olah, G. A.; Prakash, G. K.; Goeppert, A., Anthropogenic chemical carbon cycle for a sustainable future. *J Am Chem Soc* **2011,** *133* (33), 12881-98.
3. Gasser, T.; Guivarch, C.; Tachiiri, K.; Jones, C. D.; Ciais, P., Negative emissions physically needed to keep global warming below 2 degrees C. *Nat Commun* **2015,** *6*, 7958.
4. Senftle, T. P.; Carter, E. A., The Holy Grail: Chemistry Enabling an Economically Viable CO(2) Capture, Utilization, and Storage Strategy. *Acc Chem Res* **2017,** *50* (3), 472-475.
5. Appel, A. M.; Bercaw, J. E.; Bocarsly, A. B.; Dobbek, H.; DuBois, D. L.; Dupuis, M.; Ferry, J. G.; Fujita, E.; Hille, R.; Kenis, P. J.; Kerfeld, C. A.; Morris, R. H.; Peden, C. H.; Portis, A. R.; Ragsdale, S. W.; Rauchfuss, T. B.; Reek, J. N.; Seefeldt, L. C.; Thauer, R. K.; Waldrop, G. L., Frontiers, opportunities, and challenges in biochemical and chemical catalysis of CO2 fixation. *Chem Rev* **2013,** *113* (8), 6621-58.

6. Matsubara, Y.; Grills, D. C.; Kuwahara, Y., Thermodynamic Aspects of Electrocatalytic CO2 Reduction in Acetonitrile and with an Ionic Liquid as Solvent or Electrolyte. *ACS Catalysis* **2015,** *5* (11), 6440-6452.
7. Pegis, M. L.; Roberts, J. A.; Wasylenko, D. J.; Mader, E. A.; Appel, A. M.; Mayer, J. M., Standard Reduction Potentials for Oxygen and Carbon Dioxide Couples in Acetonitrile and N,N-Dimethylformamide. *Inorg Chem* **2015,** *54* (24), 11883-8.
8. Li, C. W.; Kanan, M. W., CO2 reduction at low overpotential on Cu electrodes resulting from the reduction of thick Cu2O films. *J Am Chem Soc* **2012,** *134* (17), 7231-4.
9. Nikoloudakis, E.; Lopez-Duarte, I.; Charalambidis, G.; Ladomenou, K.; Ince, M.; Coutsolelos, A. G., Porphyrins and phthalocyanines as biomimetic tools for photocatalytic H(2) production and CO(2) reduction. *Chem Soc Rev* **2022,** *51* (16), 6965-7045.
10. Costentin, C.; Robert, M.; Saveant, J. M., Catalysis of the electrochemical reduction of carbon dioxide. *Chem Soc Rev* **2013,** *42* (6), 2423-36.
11. Schouten, K. J. P.; Kwon, Y.; van der Ham, C. J. M.; Qin, Z.; Koper, M. T. M., A new mechanism for the selectivity to C1 and C2 species in the electrochemical reduction of carbon dioxide on copper electrodes. *Chemical Science* **2011,** *2* (10).
12. Asadi, M.; Kim, K.; Liu, C.; Addepalli, A. V.; Abbasi, P.; Yasaei, P.; Phillips, P.; Behranginia, A.; Cerrato, J. M.; Haasch, R.; Zapol, P.; Kumar, B.; Klie, R. F.; Abiade, J.; Curtiss, L. A.; Salehi-Khojin, A., Nanostructured transition metal dichalcogenide electrocatalysts for CO2 reduction in ionic liquid. *Science* **2016,** *353* (6298), 467-470.
13. Schneider, J.; Jia, H.; Kobiro, K.; Cabelli, D. E.; Muckerman, J. T.; Fujita, E., Nickel(ii) macrocycles: highly efficient electrocatalysts for the selective reduction of CO2 to CO. *Energy & Environmental Science* **2012,** *5* (11), 9502-9510.
14. Beley, M.; Collin, J.-P.; Ruppert, R.; Sauvage, J.-P., Nickel(II)-cyclam: an extremely selective electrocatalyst for reduction of CO2 in water. *Journal of the Chemical Society, Chemical Communications* **1984,** (19), 1315-1316.
15. Collin, J. P.; Jouaiti, A.; Sauvage, J. P., Electrocatalytic properties of (tetraazacyclotetradecane)nickel(2+) and Ni2(biscyclam)4+ with respect to carbon dioxide and water reduction. *Inorganic Chemistry* **1988,** *27* (11), 1986-1990.
16. Froehlich, J. D.; Kubiak, C. P., The homogeneous reduction of CO(2) by [Ni(cyclam)](+): increased catalytic rates with the addition of a CO scavenger. *J Am Chem Soc* **2015,** *137* (10), 3565-73.
17. Schneider, J.; Jia, H.; Muckerman, J. T.; Fujita, E., Thermodynamics and kinetics of CO2, CO, and H+ binding to the metal centre of CO2 reduction catalysts. *Chem Soc Rev* **2012,** *41* (6), 2036-51.
18. Costentin, C.; Drouet, S.; Passard, G.; Robert, M.; Savéant, J.-M., Proton-Coupled Electron Transfer Cleavage of Heavy-Atom Bonds in Electrocatalytic Processes. Cleavage of a C–O Bond in the Catalyzed Electrochemical Reduction of CO2. *Journal of the American Chemical Society* **2013,** *135* (24), 9023-9031.
19. Costentin, C.; Passard, G.; Robert, M.; Saveant, J. M., Ultraefficient homogeneous catalyst for the CO2-to-CO electrochemical conversion. *Proc Natl Acad Sci U S A* **2014,** *111* (42), 14990-4.
20. Margarit, C. G.; Schnedermann, C.; Asimow, N. G.; Nocera, D. G., Carbon Dioxide Reduction by Iron Hangman Porphyrins. *Organometallics* **2018,** *38* (6), 1219-1223.
21. Nichols, E. M.; Derrick, J. S.; Nistanaki, S. K.; Smith, P. T.; Chang, C. J., Positional effects of second-sphere amide pendants on electrochemical CO(2) reduction catalyzed by iron porphyrins. *Chem Sci* **2018,** *9* (11), 2952-2960.
22. Costentin, C.; Drouet, S.; Robert, M.; Savéant, J.-M., A Local Proton Source Enhances CO2 Electroreduction to CO by a Molecular Fe Catalyst. *Science* **2012,** *338* (6103), 90-94.
23. Amanullah, S.; Saha, P.; Dey, A., Activating the Fe(I) State of Iron Porphyrinoid with Second-Sphere Proton Transfer Residues for Selective Reduction of CO2 to HCOOH via Fe(III/II)–COOH Intermediate(s). *Journal of the American Chemical Society* **2021,** *143* (34), 13579-13592.
24. Teindl, K.; Patrick, B. O.; Nichols, E. M., Linear Free Energy Relationships and Transition State Analysis of CO2 Reduction Catalysts Bearing Second Coordination Spheres with Tunable Acidity. *Journal of the American Chemical Society* **2023,** *145* (31), 17176-17186.
25. Costentin, C.; Robert, M.; Saveant, J. M.; Tatin, A., Efficient and selective molecular catalyst for the CO2-to-CO electrochemical conversion in water. *Proc Natl Acad Sci U S A* **2015,** *112* (22), 6882-6.
26. Gotico, P.; Boitrel, B.; Guillot, R.; Sircoglou, M.; Quaranta, A.; Halime, Z.; Leibl, W.; Aukauloo, A., Second-Sphere Biomimetic Multipoint Hydrogen-Bonding Patterns to Boost CO(2) Reduction of Iron Porphyrins. *Angew Chem Int Ed Engl* **2019,** *58* (14), 4504-4509.
27. Manbeck, G. F.; Fujita, E., A review of iron and cobalt porphyrins, phthalocyanines and related complexes for electrochemical and photochemical reduction of carbon dioxide. *Journal of Porphyrins and Phthalocyanines* **2015,** *19* (01-03), 45-64.
28. Sinha, W.; Mahammed, A.; Fridman, N.; Diskin-Posner, Y.; Shimon, L. J. W.; Gross, Z., Superstructured metallocorroles for electrochemical CO(2) reduction. *Chem Commun (Camb)* **2019,** *55* (79), 11912-11915.
29. De, R.; Gonglach, S.; Paul, S.; Haas, M.; Sreejith, S. S.; Gerschel, P.; Apfel, U. P.; Vuong, T. H.; Rabeah, J.; Roy, S.; Schofberger, W., Electrocatalytic Reduction of CO(2) to Acetic Acid by a Molecular Manganese Corrole Complex. *Angew Chem Int Ed Engl* **2020,** *59* (26), 10527-10534.
30. Smieja, J. M.; Kubiak, C. P., Re(bipy-tBu)(CO)3Cl-improved catalytic activity for reduction of carbon dioxide: IR-spectroelectrochemical and mechanistic studies. *Inorg Chem* **2010,** *49* (20), 9283-9.
31. Sampson, M. D.; Nguyen, A. D.; Grice, K. A.; Moore, C. E.; Rheingold, A. L.; Kubiak, C. P., Manganese Catalysts with Bulky Bipyridine Ligands for the Electrocatalytic Reduction of Carbon Dioxide: Eliminating Dimerization and Altering Catalysis. *Journal of the American Chemical Society* **2014,** *136* (14), 5460-5471.
32. Fernandez, S.; Franco, F.; Casadevall, C.; Martin-Diaconescu, V.; Luis, J. M.; Lloret-Fillol, J., A Unified Electro- and Photocatalytic CO2 to CO Reduction Mechanism with Aminopyridine Cobalt Complexes. *J Am Chem Soc* **2020,** *142* (1), 120-133.
33. Gonell, S.; Assaf, E. A.; Lloret-Fillol, J.; Miller, A. J. M., An Iron Bis(carbene) Catalyst for Low Overpotential CO2 Electroreduction to CO: Mechanistic Insights from Kinetic Zone Diagrams, Spectroscopy, and Theory. *ACS Catalysis* **2021,** *11* (24), 15212-15222.
34. Droghetti, F.; Amati, A.; Ruggi, A.; Natali, M., Bioinspired motifs in proton and CO(2) reduction with 3d-metal polypyridine complexes. *Chem Commun (Camb)* **2024,** *60* (6), 658-673.
35. Cometto, C.; Chen, L.; Lo, P.-K.; Guo, Z.; Lau, K.-C.; Anxolabéhère-Mallart, E.; Fave, C.; Lau, T.-C.; Robert, M., Highly Selective Molecular Catalysts for the CO2-to-CO Electrochemical Conversion at Very Low Overpotential. Contrasting Fe vs Co Quaterpyridine Complexes upon Mechanistic Studies. *ACS Catalysis* **2018,** *8* (4), 3411-3417.
36. Cometto, C.; Chen, L.; Anxolabéhère-Mallart, E.; Fave, C.; Lau, T.-C.; Robert, M., Molecular Electrochemical Catalysis of the CO2-to-CO Conversion with a Co Complex: A Cyclic Voltammetry Mechanistic Investigation. *Organometallics* **2018,** *38* (6), 1280-1285.
37. Lacy, D. C.; McCrory, C. C.; Peters, J. C., Studies of cobalt-mediated electrocatalytic CO2 reduction using a redox-active ligand. *Inorg Chem* **2014,** *53* (10), 4980-8.
38. Queyriaux, N., Redox-Active Ligands in Electroassisted Catalytic H+ and CO2 Reductions: Benefits and Risks. *ACS Catalysis* **2021,** *11* (7), 4024-4035.
39. Derrick, J. S.; Loipersberger, M.; Chatterjee, R.; Iovan, D. A.; Smith, P. T.; Chakarawet, K.; Yano, J.; Long, J. R.; Head-Gordon, M.; Chang, C. J., Metal-Ligand Cooperativity via Exchange Coupling Promotes Iron- Catalyzed Electrochemical CO2 Reduction at Low Overpotentials. *J Am Chem Soc* **2020,** *142* (48), 20489-20501.
40. Rickmeyer, K.; Niederegger, L.; Keilwerth, M.; Hess, C. R., Multifaceted Role of the Noninnocent Mabiq Ligand in Promoting Selective Reduction of CO2 to CO. *ACS Catalysis* **2022,** *12* (5), 3046-3057.
41. Su, X.; McCardle, K. M.; Chen, L.; Panetier, J. A.; Jurss, J. W., Robust and Selective Cobalt Catalysts Bearing Redox-Active Bipyridyl-N-heterocyclic Carbene Frameworks for Electrochemical CO2 Reduction in Aqueous Solutions. *ACS Catalysis* **2019,** *9* (8), 7398-7408.
42. Reid, A. G.; Hooe, S. L.; Moreno, J. J.; Dickie, D. A.; Machan, C. W., Homogeneous Electrocatalytic Reduction of CO(2) by a CrN(3)O Complex: Electronic Coupling with a Redox-Active Terpyridine Fragment Favors Selectivity for CO. *Inorg Chem* **2022,** *61* (43), 16963-16970.

43. Taheri, A.; Berben, L. A., Tailoring Electrocatalysts for Selective CO2 or H(+) Reduction: Iron Carbonyl Clusters as a Case Study. *Inorg Chem* **2016,** *55* (2), 378-85.
44. Roy, S.; Sharma, B.; Pecaut, J.; Simon, P.; Fontecave, M.; Tran, P. D.; Derat, E.; Artero, V., Molecular Cobalt Complexes with Pendant Amines for Selective Electrocatalytic Reduction of Carbon Dioxide to Formic Acid. *J Am Chem Soc* **2017,** *139* (10), 3685-3696.
45. Waldie, K. M.; Ostericher, A. L.; Reineke, M. H.; Sasayama, A. F.; Kubiak, C. P., Hydricity of Transition-Metal Hydrides: Thermodynamic Considerations for CO2 Reduction. *ACS Catalysis* **2018,** *8* (2), 1313-1324.
46. Fernández, S.; Franco, F.; Martínez Belmonte, M.; Friães, S.; Royo, B.; Luis, J. M.; Lloret-Fillol, J., Decoding the CO2 Reduction Mechanism of a Highly Active Organometallic Manganese Electrocatalyst: Direct Observation of a Hydride Intermediate and Its Implications. *ACS Catalysis* **2023,** *13* (15), 10375-10385.
47. Ceballos, B. M.; Yang, J. Y., Directing the reactivity of metal hydrides for selective CO(2) reduction. *Proc Natl Acad Sci U S A* **2018,** *115* (50), 12686-12691.
48. Rakowski Dubois, M.; Dubois, D. L., Development of Molecular Electrocatalysts for CO2 Reduction and H2 Production/Oxidation. *Accounts of Chemical Research* **2009,** *42* (12), 1974-1982.
49. DuBois, D. L.; Bullock, R. M., Molecular Electrocatalysts for the Oxidation of Hydrogen and the Production of Hydrogen – The Role of Pendant Amines as Proton Relays. *European Journal of Inorganic Chemistry* **2011,** *2011* (7), 1017-1027.
50. Calvary, C. A.; Hietsoi, O.; Hofsommer, D. T.; Brun, H. C.; Costello, A. M.; Mashuta, M. S.; Spurgeon, J. M.; Buchanan, R. M.; Grapperhaus, C. A., Copper bis(thiosemicarbazone) Complexes with Pendent Polyamines: Effects of Proton Relays and Charged Moieties on Electrocatalytic HER. *European Journal of Inorganic Chemistry* **2020,** *2021* (3), 267-275.
51. Straistari, T.; Fize, J.; Shova, S.; Réglier, M.; Artero, V.; Orio, M., A Thiosemicarbazone–Nickel(II) Complex as Efficient Electrocatalyst for Hydrogen Evolution. *ChemCatChem* **2016,** *9* (12), 2262-2268.
52. Zarkadoulas, A.; Field, M. J.; Artero, V.; Mitsopoulou, C. A., Proton reduction reaction catalyzed by homoleptic nickel bis-1,2-dithiolate complexes: Experimental and theoretical mechanistic investigations. *ChemCatChem* **2017,** *9* (12), 2308-2317.
53. Solis, B. H.; Hammes-Schiffer, S., Computational study of anomalous reduction potentials for hydrogen evolution catalyzed by cobalt dithiolene complexes. *J Am Chem Soc* **2012,** *134* (37), 15253-6.
54. McNamara, W. R.; Han, Z.; Yin, C. J.; Brennessel, W. W.; Holland, P. L.; Eisenberg, R., Cobalt-dithiolene complexes for the photocatalytic and electrocatalytic reduction of protons in aqueous solutions. *Proc Natl Acad Sci U S A* **2012,** *109* (39), 15594-9.
55. Queyriaux, N.; Sun, D.; Fize, J.; Pecaut, J.; Field, M. J.; Chavarot-Kerlidou, M.; Artero, V., Electrocatalytic Hydrogen Evolution with a Cobalt Complex Bearing Pendant Proton Relays: Acid Strength and Applied Potential Govern Mechanism and Stability. *J Am Chem Soc* **2020,** *142* (1), 274-282.
56. Chapovetsky, A.; Welborn, M.; Luna, J. M.; Haiges, R.; Miller, T. F., 3rd; Marinescu, S. C., Pendant Hydrogen-Bond Donors in Cobalt Catalysts Independently Enhance CO(2) Reduction. *ACS Cent Sci* **2018,** *4* (3), 397-404.
57. Guo, H.; Liang, Z.; Guo, K.; Lei, H.; Wang, Y.; Zhang, W.; Cao, R., Iron porphyrin with appended guanidyl group for significantly improved electrocatalytic carbon dioxide reduction activity and selectivity in aqueous solutions. *Chinese Journal of Catalysis* **2022,** *43* (12), 3089-3094.
58. Kottrup, K. G.; D'Agostini, S.; van Langevelde, P. H.; Siegler, M. A.; Hetterscheid, D. G. H., Catalytic Activity of an Iron-Based Water Oxidation Catalyst: Substrate Effects of Graphitic Electrodes. *ACS Catal* **2018,** *8* (2), 1052-1061.
59. Boer, D. D.; Siberie, Q.; Siegler, M. A.; Ferber, T. H.; Moritz, D. C.; Hofmann, J. P.; Hetterscheid, D. G. H., On the Homogeneity of a Cobalt-Based Water Oxidation Catalyst. *ACS Catal* **2022,** *12* (8), 4597-4607.
60. den Boer, D.; Konovalov, A. I.; Siegler, M. A.; Hetterscheid, D. G. H., Unusual Water Oxidation Mechanism via a Redox-Active Copper Polypyridyl Complex. *Inorg Chem* **2023,** *62* (14), 5303-5314.
61. Kohler, L.; Niklas, J.; Johnson, R. C.; Zeller, M.; Poluektov, O. G.; Mulfort, K. L., Molecular Cobalt Catalysts for H(2) Generation with Redox Activity and Proton Relays in the Second Coordination Sphere. *Inorg Chem* **2019,** *58* (2), 1697-1709.
62. Droghetti, F.; Lucarini, F.; Molinari, A.; Ruggi, A.; Natali, M., Recent findings and future directions in photosynthetic hydrogen evolution using polypyridine cobalt complexes. *Dalton Trans* **2022,** *51* (28), 10658-10673.
63. Kohler, L.; Potocny, A. M.; Niklas, J.; Zeller, M.; Poluektov, O. G.; Mulfort, K. L., Replacing Pyridine with Pyrazine in Molecular Cobalt Catalysts: Effects on Electrochemical Properties and Aqueous H2 Generation. *Catalysts* **2021,** *11* (1).
64. Liu, J.; Liao, R. Z.; Heinemann, F. W.; Meyer, K.; Thummel, R. P.; Zhang, Y.; Tong, L., Electrocatalytic Hydrogen Evolution by Cobalt Complexes with a Redox Non-Innocent Polypyridine Ligand. *Inorg Chem* **2021,** *60* (23), 17976-17985.
65. Reiher, M.; Salomon, O.; Artur Hess, B., Reparameterization of hybrid functionals based on energy differences of states of different multiplicity. *Theoretical Chemistry Accounts: Theory, Computation, and Modeling (Theoretica Chimica Acta)* **2001,** *107* (1), 48-55.
66. Singh, G.; Gamboa, S.; Orio, M.; Pantazis, D. A.; Roemelt, M., Magnetic exchange coupling in Cu dimers studied with modern multireference methods and broken-symmetry coupled cluster theory. *Theoretical Chemistry Accounts* **2021,** *140* (10).
67. Meeus, E. J.; Derks, M. T. G. M.; van Leest, N. P.; Verhoef, C. J.; Roithová, J.; Reek, J. N. H.; de Bruin, B., Styrene aziridination with [CoIII(TAMLred)]– in water: Understanding and preventing epoxidation via nitrene hydrolysis. *Chem Catalysis* **2023,** *3* (8).
68. Malik, D. D.; Ryu, W.; Kim, Y.; Singh, G.; Kim, J. H.; Sankaralingam, M.; Lee, Y. M.; Seo, M. S.; Sundararajan, M.; Ocampo, D.; Roemelt, M.; Park, K.; Kim, S. H.; Baik, M. H.; Shearer, J.; Ray, K.; Fukuzumi, S.; Nam, W., Identification, Characterization, and Electronic Structures of Interconvertible Cobalt-Oxygen TAML Intermediates. *J Am Chem Soc* **2024,** *146* (20), 13817-13835.
69. Smieja, J. M.; Benson, E. E.; Kumar, B.; Grice, K. A.; Seu, C. S.; Miller, A. J.; Mayer, J. M.; Kubiak, C. P., Kinetic and structural studies, origins of selectivity, and interfacial charge transfer in the artificial photosynthesis of CO. *Proc Natl Acad Sci U S A* **2012,** *109* (39), 15646-50.
70. Dey, S.; Masero, F.; Brack, E.; Fontecave, M.; Mougel, V., Electrocatalytic metal hydride generation using CPET mediators. *Nature* **2022,** *607* (7919), 499-506.
71. Dey, S.; Todorova, T. K.; Fontecave, M.; Mougel, V., Electroreduction of CO(2) to Formate with Low Overpotential using Cobalt Pyridine Thiolate Complexes. *Angew Chem Int Ed Engl* **2020,** *59* (36), 15726-15733.
72. Li, Y.; Chen, J. Y.; Zhang, X.; Peng, Z.; Miao, Q.; Chen, W.; Xie, F.; Liao, R. Z.; Ye, S.; Tung, C. H.; Wang, W., Electrocatalytic Interconversions of CO(2) and Formate on a Versatile Iron-Thiolate Platform. *J Am Chem Soc* **2023,** *145* (49), 26915-26924.
73. Gennaro, A.; Isse, A. A.; Vianello, E., Solubility and electrochemical determination of CO2 in some dipolar aprotic solvents. *Journal of Electroanalytical Chemistry and Interfacial Electrochemistry* **1990,** *289* (1), 203-215.
74. Marx, D., Proton transfer 200 years after von Grotthuss: insights from ab initio simulations. *Chemphyschem* **2006,** *7* (9), 1848-70.
75. Hassanali, A.; Giberti, F.; Cuny, J.; Kühne, T. D.; Parrinello, M., Proton transfer through the water gossamer. *Proceedings of the National Academy of Sciences* **2013,** *110* (34), 13723-13728.
76. Ragsdale, S. W.; Kumar, M., Nickel-Containing Carbon Monoxide Dehydrogenase/Acetyl-CoA Synthase. *Chemical Reviews* **1996,** *96* (7), 2515-2540.
77. Jeoung, J.-H.; Dobbek, H., Carbon Dioxide Activation at the Ni,Fe-Cluster of Anaerobic Carbon Monoxide Dehydrogenase. *Science* **2007,** *318* (5855), 1461-1464.
78. Lubitz, W.; Ogata, H.; Rüdiger, O.; Reijerse, E., Hydrogenases. *Chemical Reviews* **2014,** *114* (8), 4081-4148.
79. Berggren, G.; Adamska, A.; Lambertz, C.; Simmons, T. R.; Esselborn, J.; Atta, M.; Gambarelli, S.; Mouesca, J. M.; Reijerse, E.; Lubitz, W.; Happe, T.; Artero, V.; Fontecave, M., Biomimetic assembly and activation of [FeFe]-hydrogenases. *Nature* **2013,** *499* (7456), 66-69.
80. Chapovetsky, A.; Do, T. H.; Haiges, R.; Takase, M. K.; Marinescu, S. C., Proton-Assisted Reduction of CO2 by Cobalt

Aminopyridine Macrocycles. *Journal of the American Chemical Society* **2016,** *138* (18), 5765-5768.
81. Beley, M.; Collin, J. P.; Ruppert, R.; Sauvage, J. P., Electrocatalytic reduction of carbon dioxide by nickel cyclam2+ in water: study of the factors affecting the efficiency and the selectivity of the process. *Journal of the American Chemical Society* **1986,** *108* (24), 7461-7467.
82. Chapovetsky, A.; Welborn, M.; Luna, J. M.; Haiges, R.; Miller, T. F., III; Marinescu, S. C., Pendant Hydrogen-Bond Donors in Cobalt Catalysts Independently Enhance CO2 Reduction. *ACS Central Science* **2018,** *4* (3), 397-404.
83. Rakowski DuBois, M.; DuBois, D. L., The roles of the first and second coordination spheres in the design of molecular catalysts for H2 production and oxidation. *Chemical Society Reviews* **2009,** *38* (1), 62-72.

Table of Contents (TOC)

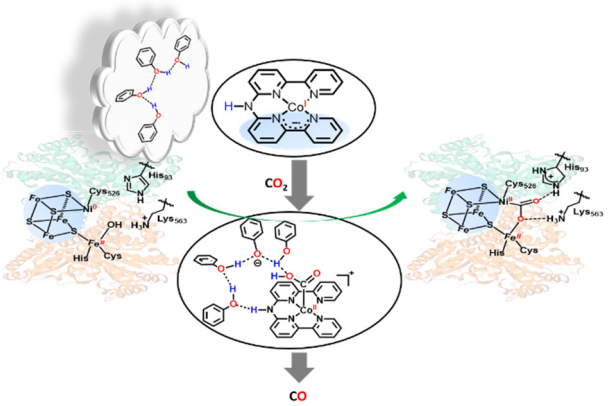

- Redox active ligand mimicking [Fe_3S_4] cluster of the enzyme
- Fast direct 2e$^-$ reduction of CO_2 faciliated by proton channel